

Accepted to ApJ on 2007 September 17

## Candidate Rotating Toroids around High-Mass (Proto)Stars

R. S. Furuya<sup>1</sup>

*Subaru Telescope, National Astronomical Observatory of Japan*

`rsf@subaru.naoj.org`

R. Cesaroni<sup>2</sup>

*INAF, Osservatorio Astrofisico di Arcetri*

`cesa@arcetri.astro.it`

S. Takahashi<sup>3</sup>

*Department of Astronomical Science, Graduate University for Advanced Studies*

`satoko_t@asiaa.sinica.edu.tw`

C. Codella<sup>2</sup>

*INAF – Istituto di Radioastronomia, Sezione di Firenze*

`codella@arcetri.astro.it`

M. Momose<sup>4</sup>

*Institute of Astronomy and Planetary Science, Ibaraki University*

`momose@mx.ibaraki.ac.jp`

and

M. T. Beltrán<sup>5</sup>

*Department d'Astronomia i Meteorologia, Universitat de Barcelona*

`mbeltran@am.ub.es`

## ABSTRACT

Using the OVRO, Nobeyama, and IRAM mm-arrays, we searched for “disk”-outflow systems in three high-mass (proto)star forming regions: G 16.59–0.05, G 23.01–0.41, and G 28.87+0.07. These were selected from a sample of  $\text{NH}_3$  cores (Codella, Testi & Cesaroni) associated with OH and  $\text{H}_2\text{O}$  maser emission (Foster & Caswell) and with no or very faint continuum emission. Our imaging of molecular line (including rotational transitions of  $\text{CH}_3\text{CN}$ ) and 3 mm dust continuum emission revealed that these are compact ( $\lesssim 0.05 - 0.3$  pc), massive ( $\sim 100 - 400 M_\odot$ ), and hot ( $\sim 100$  K) molecular cores (HMCs), that is likely sites of high-mass star formation prior to the appearance of ultracompact HII regions. All three sources turn out to be associated with molecular outflows from  $^{12}\text{CO}$  and/or  $\text{HCO}^+$   $J=1-0$  line imaging. In addition, velocity gradients of  $10 - 100 \text{ km s}^{-1} \text{ pc}^{-1}$  in the innermost ( $\lesssim 0.03 - 0.13$  pc), densest regions of the G 23.01–0.41 and G 28.87+0.07 HMCs are identified along directions roughly perpendicular to the axes of the corresponding outflows. All the results suggest that these cores might be rotating about the outflow axis, although the contribution of rotation to gravitational equilibrium of the HMCs appears to be negligible. Our analysis indicates that the 3 HMCs are close to virial equilibrium due to turbulent pressure support. Comparison with other similar objects where rotating toroids have been identified so far shows that in our case rotation appears to be much less prominent; this can be explained by the combined effect of unfavorable projection, large distance, and limited angular resolution with the current interferometers.

*Subject headings:* ISM: evolution — ISM: individual (G 16.59–0.05, G 23.01–0.41, G 28.87+0.07) — stars: early type — radio continuum: ISM

---

<sup>1</sup>650 North A’ohoku Place, Hilo, HI 96720

<sup>2</sup>Largo Enrico Fermi 5, I-50125 Firenze, Italy

<sup>3</sup>Current address: Academia Sinica Institute of Astronomy and Astrophysics, P.O. Box 23-141, Taipei 106, Taiwan, R.O.C.

<sup>5</sup>Bunkyo 2-1-1, Mito, Ibaraki 310-8512, Japan

<sup>6</sup>Av. Diagonal, 647, 08028, Barcelona, Catalunya, Spain

## 1. Introduction

The role of disks in the formation process of low-mass stars (i.e. stars with masses  $\lesssim 1 M_{\odot}$ ) has been extensively studied in the last two decades through high angular resolution observations at various wavelengths. Images of such disks have been obtained in the optical (e.g. Burrows et al. 1996) and at mm-wavelengths (e.g. Simon et al. 2000). The latter have demonstrated that the majority of the disks undergo Keplerian rotation. These findings are consistent with the fact that low-mass stars form through accretion while (partial) conservation of angular momentum during the dynamical collapse produces a flattened and rotating structure at the center of the core.

What about high-mass ( $M_* \gtrsim 8 M_{\odot}$ ) stars? In this case, formation through accretion faces the problem that stars more massive than  $\sim 8 M_{\odot}$  reach the zero age main sequence still deeply embedded in their parental cores (Palla & Stahler 1993). At this point radiation pressure from the newly formed early-type star can halt the infall, thus preventing further growth of the stellar mass. Various solutions have been proposed to solve this problem: (i) massive stars might form through merging of lower mass stars (Bonnell, Bate & Zinnecker, H. 1998; Bonnell & Bate 2002; Bally & Zinnecker 2005); (ii) sufficiently large accretion rates could allow the ram pressure of the infalling material to overcome the radiation pressure from the star (Behrend & Maeder 2001; McKee & Tan 2003; Bonnell, Vine, & Bate 2004) (iii) non-spherical accretion could weaken the effect of radiation pressure by allowing part of the photons to escape through evacuated regions along the outflow axis and, at the same time, enhancing the ram pressure of the accreting material by focusing it through the disk plane (Yorke & Sonnhalter 2002; Krumholz, McKee, & Klein 2005).

An important test to discriminate between the different hypotheses is the presence of rotating, circumstellar disks, which would lend support to the third scenario depicted above. This can be determined by inspecting the velocity field of the innermost parts of molecular cores where young massive (proto)stars are believed to form. One possibility is to look for velocity gradients perpendicular to the direction of the larger scale outflows associated with such cores; this would suggest that one is observing rotation about the outflow axis. This technique has been adopted by us and other authors successfully inferring the existence of rotation in the gas enshrouding high-mass young stellar objects (YSOs) and leading to the discovery of circumstellar disk-like structure or “toroids” in a limited number of cases (see Cesaroni et al. 2007 for a review on this topic).

The goal of the present study was to establish whether the presence of rotation is common in high-mass star forming regions by observing three more objects, expected to be sites of deeply embedded OB (proto)stars. The ideal target for this type of studies are hot molecular cores (HMCs), which are believed to be the cradles of massive stars (see e.g.

Kurtz et al. 2000; Cesaroni et al. 2007). Beside other studies, the one by Codella, Testi & Cesaroni (1997, hereafter CTC97), has proved successful in identifying the birthplaces of young massive stars as dense  $\text{NH}_3$  cores associated with OH and  $\text{H}_2\text{O}$  maser emission. One of these HMCs (G 24.78+0.08) has been the subject of a series of articles by us (Furuya et al. 2002; Cesaroni et al. 2003; Beltrán et al. 2004, 2005), which have shown that this is a unique object, characterized by the simultaneous presence of rotation, outflow, and infall towards a hypercompact HII region ionized by an O9.5 star (Beltrán et al. 2006). With this in mind, we completed the study of the sources in CTC97 by observing three more objects in the same tracers used to investigate G 24.78+0.08. The selected targets for this study are G 16.59–0.05 at  $d = 4.7$  kpc, G 28.87+0.07 at 7.4 kpc, and G 23.01–0.41 at 10.7 kpc. The fact that in all three cases no or only faint free-free continuum emission has been detected, notwithstanding the large luminosities of the sources (CTC97), suggests that the embedded YSOs might be in an even earlier evolutionary phase than those in G 24.78+0.08 (Furuya et al. 2002; Beltrán et al. 2004).

## 2. Observations and Data Retrieval

### 2.1. Millimeter Array Observations

Aperture synthesis observations of molecular lines and continuum emission at 3 mm were carried out using the Owens Valley Radio Observatory (OVRO)<sup>1</sup> millimeter array towards G 16.59–0.05 and G 28.87+0.07, and the Nobeyama Millimeter Array (NMA) of the Nobeyama Radio Observatory<sup>2</sup> towards G 23.01–0.41. We also carried out  $^{12}\text{CO}$  (1–0) line and millimeter continuum emission imaging with the Plateau de Bure Interferometer (PdBI) of the Institut de Radio Astronomie Millimétrique<sup>3</sup> (IRAM). The parameters for the continuum and molecular line observations are summarized in Tables 1 and 2, respectively.

---

<sup>1</sup>Research at the Owens Valley Radio Observatory is supported by the National Science Foundation through NSF grant AST 02-28955.

<sup>2</sup>Nobeyama Radio Observatory is a branch of the National Astronomical Observatory, operated by the Ministry of Education, Culture, Sports, Science and Technology, Japan.

<sup>3</sup>IRAM is supported by INSU/CNRS (France), MPG (Germany), and IGN (Spain).

### 2.1.1. OVRO Observations

The OVRO observations of G 16.59–0.05 and G 28.87+0.07 were carried out in the period from 2003 September to 2004 May in 3 array configurations (E, H, and UH). The shortest projected baseline length, i.e. the shadowing limit, is about 12.8 m. This makes our OVRO observations insensitive to structures more extended than  $54''$ , corresponding to 1.2 and 1.9 pc at the distances of G 16.59–0.05 and G 28.87+0.07, respectively. We observed the  $\text{CH}_3\text{CN}$  (5–4) and  $\text{N}_2\text{H}^+$  (1–0) lines in the upper sideband (USB) and the  $\text{HCO}^+$  (1–0) line in the lower sideband (LSB). For the continuum emission, we simultaneously used the Continuum Correlator with an effective bandwidth of 4 GHz and the newly installed COBRA with 8 GHz bandwidth. We configured the digital correlator with 31 MHz bandwidth and 62 channels centered at 91979.970 MHz, so to cover the  $K = 0$  to 3 components of the  $\text{CH}_3\text{CN}$  (5–4) transition. We used 3C 273 and 3C 454.3 as passband calibrators, and NRAO 530 and J1743–038 as phase and gain calibrators respectively for G 16.59–0.05 and G 28.87+0.07. The flux densities of NRAO 530 and J1743–038 were determined from observations of Uranus and Neptune. We estimate the uncertainty of flux calibrations to be 10%. The data were calibrated and edited using the MMA and MIRIAD packages. We constructed continuum images from the COBRA data by employing the multi-frequency synthesis method: the final center frequency is 90.584 GHz.

### 2.1.2. NMA Observations

Our NMA observations towards G 23.01–0.41 were carried out in the period from 2003 December to 2004 May with 3 array configurations (D, C, and AB). The largest detectable source size is  $50''$ , corresponding to 2.6 pc at  $d = 10.7$  kpc. We observed the  $\text{CH}_3\text{CN}$  (6–5),  $\text{HNCO}$  (5–4),  $^{13}\text{CO}$  (1–0) and  $\text{C}^{18}\text{O}$  (1–0) lines in the USB. For the continuum and line emission, except for  $\text{CH}_3\text{CN}$ , we employed the Ultra Wide Band Correlator (UWBC) with a 512 MHz bandwidth in each sideband; this configuration gives a total bandwidth of 1 GHz for the continuum and a velocity resolution of  $5.5 \text{ km s}^{-1}$  for the lines. We used the FX correlator with 32 MHz bandwidth centered at 110374.0 MHz, thus covering the  $K = 0$  to 3 components of the  $\text{CH}_3\text{CN}$  (6–5) transition. We adopted 3C 273 as passband calibrator and J1743–038 as phase and gain calibrator. The flux densities of J1743–038 were bootstrapped from Uranus, and the uncertainty of the flux calibration is estimated to be 10%. We decided not to use the  $^{13}\text{CO}$  and  $\text{C}^{18}\text{O}$  data taken with the C and AB configurations as these are too extended and resolve the emission. All the data were calibrated and edited using the UVPROC2 and MIRIAD packages.

### 2.1.3. PdBI Observations

Our  $^{12}\text{CO}$  (1–0) and 2.6 mm continuum emission observations towards the 3 HMCs were carried out with the IRAM 5-antenna interferometer on Plateau de Bure in 1998 April and May. The D and C1 configurations were used, yielding a largest detectable angular scale of  $\sim 44''$ . The 82 – 116 GHz SIS receivers were tuned in SSB at the frequency of the  $^{12}\text{CO}$  (1–0) line, and the facility correlator was configured with a bandwidth of 40 MHz centered at the same frequency. Continuum emission has also been measured with two bandwidths of 160 MHz each. Line free channels were averaged to produce a continuum image which was then subtracted from the line data in the visibility plane. The flux densities of J1833–210 (1.7 Jy) and J1743–038 (3.0 Jy) were bootstrapped from 3C 273 whose flux density was assumed to be 16.7 Jy. We estimated an overall uncertainty on flux calibration of 20%. Data editing, calibrations, and image construction were done using the GILDAS software package developed at IRAM. Tables 1 and 2 summarize the observing parameters for the PdBI continuum and line imaging, respectively.

## 2.2. GLIMPSE and MSX Archive Data

We have retrieved infrared (IR) images at  $21\ \mu\text{m}$  from the Midcourse Space Experiment (MSX; Price et al. 2001) survey and at 8.0, 5.8, 4.5, and  $3.6\ \mu\text{m}$  from the Galactic Legacy Infrared Mid-Plane Survey (GLIMPSE) survey making use of the Infrared Array Camera (IRAC) on-board the *Spitzer* satellite. The calibrated data from the *Spitzer Science Center* were processed through the GLIMPSE pipeline reduction system (Benjamin et al. 2003; Whitney et al. 2004). All the infrared (IR) images were used without spatial smoothing; the pixel size is  $6''$  and  $\sim 1''.2$  for the MSX and IRAC data, respectively.

## 3. Results and Discussion

### 3.1. Continuum Emission

#### 3.1.1. Source Identification Based on Millimeter Images

Figure 1 compares our 3 mm continuum emission maps to the IR images. The latter correspond to the MSX data at  $21\ \mu\text{m}$  and the GLIMPSE ones at the longest ( $8.0\ \mu\text{m}$ ) and shortest ( $3.6\ \mu\text{m}$ ) wavelengths. Here we do not show GLIMPSE images at 5.8 and  $4.5\ \mu\text{m}$  as they are basically similar to those at 8.0 and  $3.6\ \mu\text{m}$ . All 3 objects show intense, compact 3 mm continuum emission coincident with IR emission, although one must consider that the

angular resolution of the MSX images is much worse than that of our interferometric maps. In the millimeter maps of G 28.87+0.07, one can also see weaker 3.3 mm continuum sources located  $\simeq 14''$  to the north (hereafter G 28.87+0.07B and C; see Figure 1b) and a 2.6 mm source  $\simeq 10''$  to the east (G 28.87+0.07D; same figure) of the main core found by CTC97. No other mm continuum emission is detected with  $S/N \geq 5$  in our OVRO, NMA, and PdBI fields of view towards the 3 sources. Assuming that the flux density  $S_\nu$ , varies as  $\nu^{(2+\beta)}$  with  $\beta = 1.5$  (Preibisch 1993; Molinari et al. 2000), the expected flux of G 28.87+0.07 B and C in the PdBI beam at 2.6 mm is below the sensitivity of our images (3.5 mJy corresponding to  $2.2\sigma$ ). Similarly, assuming that G 28.87+0.07 D matches the PdBI beam, this source is resolved by the OVRO beam and its flux at 3.3 mm corresponds to only  $1.4\sigma$  of the OVRO continuum image, thus explaining why it is not detected.

The GLIMPSE images of G 16.59–0.05 and G 28.87+0.07 show IR emission both from the main cores and from their surroundings. On the other hand, G 23.01–0.41 seems rather isolated, although we may be missing weaker objects due to the large distance to the region. In the following we make no attempt to identify other IR sources beside the counterparts of those detected at mm wavelengths, because this would require an analysis which goes beyond the purposes of the present study. Notice that no other mm sources with  $3 \leq S/N < 5$  is seen in the IRAC bands. We summarized the identified continuum sources in Table 3, where peak positions and effective radius ( $R_{\text{eff}}$ ) of the mm-continuum sources as well as their  $S_\nu$  integrated inside the  $5\sigma$  level contours are given. Here the observed angular radius of the source is computed from  $\sqrt{\mathcal{A}/\pi}$  where  $\mathcal{A}$  is the area enclosed by the 50% contour level of the emission. Deconvolution assuming the source and the synthesized beam to be Gaussian is then applied, thus obtaining  $R_{\text{eff}}$ , assuming that the emission has a Gaussian distribution. It should be noted that  $R_{\text{eff}}$  does not depend on the image noise levels. To estimate the core mass from the continuum flux the latter has been integrated all over the emitting region, namely inside the corresponding  $5\sigma$  contour level. The fluxes of the IR counterparts are listed in Table 4.

### 3.1.2. Continuum Spectra and Core Masses Estimated from the 3 mm Flux Densities

Figure 2 shows the continuum spectra of the 3 HMCs, as from Tables 3 and 4. No contamination by free-free emission is expected to affect our 3 mm fluxes, as the upper limits obtained by CTC97 at 1.26 cm guarantee a maximum free-free flux of  $\simeq 1.4$  mJy at 3.0 mm – assuming optically thin emission. Establishing the origin of the IR emission requires a model fitting of the spectral energy distribution (SED) that goes beyond the purpose of this study. We only note that a simple grey-body fit cannot consistently reproduce the SED

from the mm to the near-IR regime. This suggests that the structure of the cores is rather complex, probably hosting a multiple stellar system such as the one seen in the G 29.96–0.02 star forming region: here, recent sub-arcsecond resolution ( $\sim 1800$  AU resolution in linear scale) Submillimeter Array (SMA) imaging resolved the HMC (Maxia et al. 2001; Olmi et al. 2003) into six submm continuum sources (Beuther et al. 2007). Although our angular resolutions in AU are 5–12 times worse, by analogy to the case of G 29.96–0.02, we may argue that multiple sources are present in our cores, which might explain why the SEDs cannot be fitted with a simple grey-body fit. Furthermore, temperature gradients as well as optical depth effects and clumpiness should be taken into account to obtain a satisfactory fit. In particular images with arcsecond resolution at wavelengths above  $20 \mu\text{m}$  would be of great importance to obtain a precise estimate of the bolometric luminosity (and hence of the mass) of the embedded (proto)stars.

The 3 mm flux density in Table 3 can be used to estimate the mass of the cores ( $M_{\text{dust}}$ ), under a few assumptions on the dust emissivity. More specifically, we use Hildebrand’s (1983) relation  $M_{\text{dust}} = \frac{S_{\nu} d^2}{\kappa_{\nu} B_{\nu}(T_{\text{dust}})}$  with  $\kappa_{\nu} = 5.0 \times 10^{-3} (\nu/231 \text{ GHz})^{\beta} \text{ cm}^2 \text{ g}^{-1}$  and  $\beta = 1.5$ . When calculating  $M_{\text{dust}}$ , we set  $T_{\text{dust}}$  equal to the rotational temperature obtained from the  $\text{CH}_3\text{CN}$  lines (see §3.5.1), assuming that gas and dust are well-coupled (e.g., Krügel & Walmsley 1984), a reasonable hypothesis at densities as high as those traced by the  $\text{CH}_3\text{CN}$  emission (typically  $> 10^{6-7} \text{ cm}^{-3}$ ).

The derived values of  $M_{\text{dust}}$  range from 95 to  $380 M_{\odot}$  (Table 5). Our 3 targets appear to fall in the mass range for “heavy” HMCs ( $\gtrsim 100 M_{\odot}$ ; Cesaroni et al. 2007). Cores that massive are likely to host multiple stars, as opposed to “light” HMCs ( $< \text{a few } 10 M_{\odot}$ ), which appear to contain only single OB stars or binary systems (Cesaroni et al. 2007).

In G 28.87+0.07 we have identified 3 additional weaker sources. Assuming that  $T_{\text{dust}}$  is equal to the excitation temperature of  $\text{N}_2\text{H}^+(1-0)$  (see §3.3.2 and Figure 5c), we obtain  $M_{\text{dust}} = 7 M_{\odot}$  with  $T_{\text{dust}} = 46 \text{ K}$  for G 28.87+0.07D. The excitation temperature is estimated from the hyperfine structure analysis of mean spectra of the  $\text{N}_2\text{H}^+$  emission towards a condensation hosting G 28.87+0.07D. If we assume that  $T_{\text{dust}} \simeq 46 \text{ K}$  is valid for G 28.87+0.07B and C, we obtain  $M_{\text{dust}}$  of  $29 M_{\odot}$  for G 28.87+0.07B and  $28 M_{\odot}$  for G 28.87+0.07C. These results suggest that the G 28.87+0.07 HMC ( $M_{\text{dust}} = 100 M_{\odot}$ ; Table 5) is surrounded by less massive objects. Such a situation appears to be typical of high-mass star forming regions, where embedded OB (proto)stars happen to be surrounded by less embedded, possibly more evolved, lower mass stars (Molinari et al. 1998; Fontani et al. 2004a, 2004b). Furthermore, because of the absence of free-free emission (CTC97), we argue that the G 28.87+0.07 cluster is much younger than other clusters of massive YSOs, such as, e.g., the cluster of ultracompact HII regions in G 19.61–0.23 (Furuya et al. 2005).



Finally, in order to estimate the  $\text{CH}_3\text{CN}$  abundance in the cores (see §3.5.2), we have calculated the mean molecular hydrogen column density,  $\langle N(\text{H}_2) \rangle$ , over the cores. To make the comparison between continuum and  $\text{CH}_3\text{CN}$  emission as consistent as possible, we re-constructed the 3 mm images by fixing the beam sizes to those of the  $\text{CH}_3\text{CN}$  images (Table 2). We subsequently integrated the continuum flux over the region enclosed by the  $5\sigma$  level contours. In Table 5 we summarize the calculated mean column densities ( $\langle N(\text{H}_2) \rangle$ ) which are  $(3 - 4) \times 10^{23} \text{ cm}^{-2}$ , implying optical depths on the order of  $10^{-3}$ , consistent with our assumption that the dust emission is optically thin at 3 mm.

### 3.2. Spectral Line Profiles towards the Cores

Figure 3 shows the line spectra at the peak positions of each integrated intensity map, in units of brightness temperature in the synthesized beam ( $T_{\text{sb}}$ ). For the  $\text{CH}_3\text{CN}$  emission, we show the  $K = 3$  component as this is not blended with the other  $K$ -ladder lines.

**G 16.59–0.06** The  $^{12}\text{CO}$  and  $\text{HCO}^+$  peak spectra present deep “absorption” features around the systemic velocity, the latter being estimated from the  $\text{CH}_3\text{CN}$  lines (see §3.5.1). Most likely this is not due to real self-absorption but to the fact that emission at low velocities arises from extended regions resolved out by the interferometer, as found in the case of G24.78+0.08 (see Cesaroni et al. 2003). However, only single-dish mapping of the regions under study in the same lines can establish the nature of such absorption.

The  $^{12}\text{CO}$  spectrum shows prominent high-velocity wings on both sides of the line, indicating the presence of a molecular outflow. In order to adopt suitable velocity ranges for the outflow lobes traced by the  $^{12}\text{CO}$  emission, we define terminal ( $V_t$ ) and boundary ( $V_b$ ) velocities:  $V_t$  is the most blue- and redshifted LSR-velocity where the wing emission drops below the  $1.5\sigma$  level and  $V_b$ ’s are the velocities where the intensity of the  $\text{CH}_3\text{CN}$   $K = 3$  line falls below  $1.5\sigma$  (see caption of Figure 4 for the  $V_t$  and  $V_b$  values).

**G 28.87+0.08** The  $^{12}\text{CO}$  and  $\text{HCO}^+$  (1–0) spectra towards G 28.87+0.07 are very similar each other in the sense that the emission around  $V_{\text{sys}}$  is almost missing, and the blueshifted wing is barely detected, whereas prominent redshifted emission is seen. The  $\text{CH}_3\text{CN}$   $K = 3$  emission peaks around  $V_{\text{LSR}} \simeq 103 \text{ km s}^{-1}$  where the  $^{12}\text{CO}$  and  $\text{HCO}^+$  spectra present a sharp edge. Also in this case, as for G 16.59–0.05, we argue that the spectral profiles of the  $^{12}\text{CO}$  and  $\text{HCO}^+$  lines may suffer of missing short spacing in our interferometric observations.

**G 23.01–0.41** The profile of the  $^{12}\text{CO}$  line towards G 23.01–0.41 presents a redshifted wing much more prominent than the blue one, while the emission close to  $V_{\text{sys}}$  is strongly depressed. On the other hand, the lines of the lower density tracers  $^{13}\text{CO}$  and  $\text{C}^{18}\text{O}$  present well defined peaks, although the velocity resolutions are poor. The peak LSR-velocities of the  $^{13}\text{CO}$  and  $\text{C}^{18}\text{O}$  emission shifted slightly towards the blue with respect to the peak velocity of  $\text{CH}_3\text{CN}$  – which we have assumed as representative of the bulk material.

### 3.3. Maps of the Molecular Line Emission

#### 3.3.1. G 16.59–0.06

Figure 4 compares maps of molecular line and continuum emission in G 16.59–0.05. Panel (a) shows an overlay of the  $^{12}\text{CO}$  wing emission on the 3 mm continuum emission. The wing emission is integrated over the velocity ranges between  $V_b$  and  $V_t$  for both the blue and red lobes (§3.2). The G 16.59–0.05 outflow map shows a clear bipolarity along a line with  $\text{P.A.} \simeq 135^\circ$ . We define the outflow axis as the line connecting the peaks of the blue lobe and 3 mm continuum map. The blue lobe shows a remarkable structure with a large opening angle of  $\simeq 180^\circ$ , whereas the red lobe is much more collimated. Interestingly, both lobes have a large aspect ratio ( $> 1$ ), defined as the ratio between the width and the length of the lobe. Moreover, the two lobes have a rather large spatial overlap, coinciding also with the position of the 3 mm continuum emission. Such a geometry indicates that the inclination angle of the outflow axis with respect to the line-of-sight – albeit difficult to quantify precisely – must be rather small.

In Figure 4d, we see that, while the distributions of  $\text{CH}_3\text{CN}$  (5–4)  $K = 0 + 1$  and  $\text{NH}_3$  (3,3) emission agree well with each other, the peak position of the 3.3 mm source is displaced by  $\simeq 1''.4$  to the northwest of the  $\text{CH}_3\text{CN}$  peak. We also verified that the peak positions of the  $K = 2$  and 3 emission agree with that of the  $K = 0 + 1$  emission. Note that the 3.3 mm continuum and  $\text{CH}_3\text{CN}$  visibilities shared the same calibrators as they were observed simultaneously (§2.1.1), and that the peak positions of the 3.3 and 2.6 mm continuum sources (see Table 3), measured respectively with OVRO and PdBI, agree with each other within the errors. These facts indicate that the positional displacement between the  $\text{CH}_3\text{CN}$  and 3 mm continuum emission is real (see §3.6 for a discussion). One cannot rule out the possibility that such a displacement is due to optical depth effects, although this seems unlikely as line emission peaks at the same position for all species ( $\text{NH}_3$  and  $\text{CH}_3\text{CN}$ ), and the  $\text{CH}_3\text{CN}$  opacity quite low ( $\lesssim 2$ ; described in §3.5.1). Observation of higher-excitation  $\text{CH}_3\text{CN}$  lines might help shedding light on this issue. The peak position of the more extended  $\text{HCO}^+$  emission agrees with those of  $\text{NH}_3$  and  $\text{CH}_3\text{CN}$ , suggesting that the  $\text{HCO}^+$  (1–0) line also

traces the HMC. On the other hand, the  $\text{N}_2\text{H}^+$  emission has a totally different morphology from the other molecules, in the sense that it has a fairly extended structure and its peak position differs from both those of the other lines and that of the 3 mm continuum. The  $\text{N}_2\text{H}^+$  emission is more extended than the  $\text{HCO}^+$  emission, suggesting that it might be associated not only with the HMC, but also with the other sources seen in the IR images (Figure 1a).

To estimate the column density of the region, we analyzed the  $\text{HCO}^+$  and  $\text{N}_2\text{H}^+$  data in the following fashion. The mean column density of a linear rigid rotor is calculated from Eq. (A1) of Scoville et al. (1986). Since we do not have measurements of the optical depth ( $\tau$ ) and excitation temperature ( $T_{\text{ex}}$ ) of the  $\text{HCO}^+$  line, we assumed that the  $\text{HCO}^+$  emission is optically thin and estimated the column density for two extreme values  $T_{\text{ex}}$ : a minimum  $T_{\text{ex}}$ , obtained from the line peak  $T_{\text{sb}}$  (32.8 K from Figure 3a) and a maximum  $T_{\text{ex}}$ , from  $T_{\text{rot}}$  of the  $\text{CH}_3\text{CN}$  emission (130 K; described in §3.5.1). Correspondingly, the mean  $\text{HCO}^+$  column density over a region enclosed by its  $5\sigma$  contour level is  $N_{\text{HCO}^+} \simeq 6.3 \times 10^{14} \text{ cm}^{-2}$  and  $2.1 \times 10^{15} \text{ cm}^{-2}$ . For the fractional abundance,  $X(\text{HCO}^+)$ , we assume a value of  $10^{-9}$  (see e.g. van Dishoeck et al. 1993). Under this assumption, the mass traced by the  $\text{HCO}^+$  (1–0) line ( $M_{\text{LTE}}$ ) ranges from 440 to 1500  $M_{\odot}$  (Table 6). We stress that these estimates are to be taken as lower limits, as part of the line emission close to the systemic velocity is resolved out in our interferometric maps.

Subsequently we analyzed the  $\text{N}_2\text{H}^+$  data because the hyperfine structure (HFS) of the transition allows an estimate of the line optical depth (see, e.g., Benson, Caselli & Myers 1998; Caselli et al. 2002). The details of our  $\text{N}_2\text{H}^+$  HFS analysis are described in Appendix B of Furuya et al. (2006). For this purpose, we used two spectra obtained integrating the emission over the  $5\sigma$  contour level of the 3 mm continuum emission and the integrated  $\text{N}_2\text{H}^+$  line emission. Note that the  $\text{N}_2\text{H}^+$  emission does not peak at the position of the 3 mm continuum source. For the first spectrum, our analysis gives  $T_{\text{ex}} \simeq 41 \pm 9 \text{ K}$ , total optical depth (corresponding to the sum of the optical depths of the 7 hyperfine components)  $\tau_{\text{tot}} \simeq 0.28 \pm 0.03$ , and intrinsic line width  $\Delta v_{\text{int}} \simeq 2.10 \pm 0.04 \text{ km s}^{-1}$  towards the 3 mm source. From the second spectrum, we obtain  $T_{\text{ex}} = 16 \pm 2 \text{ K}$ ,  $\tau_{\text{tot}} = 0.91$  and  $\Delta v_{\text{int}} = 2.82 \pm 0.02 \text{ km s}^{-1}$ . Using Eq. (B7) of Furuya et al. (2006), we calculate a column density  $N_{\text{N}_2\text{H}^+} \simeq (7.8 \pm 1.5) \times 10^{13} \text{ cm}^{-2}$  towards the 3 mm continuum source and  $(6.1 \pm 0.4) \times 10^{13} \text{ cm}^{-2}$  for the average spectrum. If we assume  $X(\text{N}_2\text{H}^+) = 3 \times 10^{-10}$  suitable for high-mass star forming regions (Womack et al. 1992), the mass estimate for the entire region is 540  $M_{\odot}$  (Table 6).

These numbers demonstrate that the  $\text{N}_2\text{H}^+$  line is coming from a lower (column) density region, distinct from the HMC traced by the continuum and  $\text{CH}_3\text{CN}$  line emission – whose analysis we defer to §3.5. This is especially evident from the line width, which for the  $\text{N}_2\text{H}^+$

line is  $\sim 50\%$  of that of the  $\text{CH}_3\text{CN}$  transitions (see Table 8).

### 3.3.2. *G 28.87+0.06*

The  $^{12}\text{CO}$  spectrum of G 28.87+0.07 strongly suggests the presence of high-velocity outflowing gas (§3.2). However, the maps of the wing emission presented in Figure 5a do not seem to outline a clear bipolar structure with respect to the 3 mm source position. A prominent red lobe lies to the southwest, whereas the blue lobe shows an elongated structure aligned approximately east-west as well as a condensation to the northeast of the main core. If we assume that all the CO lobe is associated with an outflow powered by a source in the core, the observed morphology and velocity structure can be interpreted in two ways: (i) one outflow, with patchy emission from the lobes and with a large opening angle (close to  $90^\circ$ ) around the axis denoted by the solid line in Figure 5a; (ii) two outflows, well collimated along the axes represented by the dashed lines in the same figure. On the basis of the present data it is impossible to discriminate between these two hypotheses. Given the existence of several sources in G 28.87+0.07 (§3.1.1) and the fact that multiple outflows appear to be frequent in high-mass star forming regions (see Beuther et al. 2002b, 2003, 2004), one cannot rule out the possibility that the blueshifted condensation to the northeast and some portion of the eastern blueshifted lobe are associated respectively with G 28.87+0.07B (and/or C) and D. However, for the sake of simplicity, in the following we will consider only the two scenarios proposed above, which assume that it is the main G 28.87+0.07 core to host the source(s) powering the outflow(s).

In G 28.87+0.07, the peak positions of all tracers but  $\text{N}_2\text{H}^+$  roughly coincide with the 3 mm continuum peak (Figure 5d). Both the  $\text{NH}_3$  and  $\text{CH}_3\text{CN}$  emission are compact, whereas the  $\text{HCO}^+$  emission is slightly elongated in the north-south direction (Figure 5b). We believe that the  $\text{HCO}^+$  emission mostly arises from the HMC and not from the outflow lobes because its elongation is not parallel to any of the possible outflow axes and only very faint  $\text{HCO}^+$  line wings are detected (see Figure 3b). As done for G 16.59–0.05, we estimate  $N_{\text{HCO}^+}$  for the region enclosed by the  $5\sigma$  level contour assuming two extreme values for the excitation temperature. We obtain  $N_{\text{HCO}^+} = 3.9 \times 10^{14} \text{ cm}^{-2}$  for  $T_{\text{ex}} = 96 \text{ K}$ , and  $9.2 \times 10^{13} \text{ cm}^{-2}$  for  $T_{\text{ex}} = 17 \text{ K}$ , yielding a mass range  $M_{\text{LTE}} \simeq 84 - 360 M_\odot$  (Table 6). Here, the maximum  $T_{\text{ex}}$  is assumed equal to the value of  $T_{\text{rot}}$  obtained from the  $\text{CH}_3\text{CN}$  emission. On the other hand, the minimum  $T_{\text{ex}}$  is taken equal to the peak  $T_{\text{sb}}$  of the  $\text{HCO}^+$  spectrum [14.5 K from Figure 3;  $T_{\text{ex}} \simeq T_{\text{sb}}^{\text{peak}}(\text{HCO}^+) + T_{\text{bg}} = 17 \text{ K}$ , where  $T_{\text{bg}}$  is the cosmic background temperature]. Independently of the value chosen, this estimate represents a lower limit because of the different UV coverages, beam dilutions, and optical depth effects. We stress that the

estimated  $N_{\text{HCO}^+}$  varies only by a factor of 4.3 regardless of the large uncertainty on  $T_{\text{ex}}$ .

It is interesting that the  $\text{N}_2\text{H}^+$  emission in G 28.87+0.07 cannot be seen towards the center of the main core, where instead  $\text{NH}_3$  emission is detected (CTC97). The distribution of the  $\text{N}_2\text{H}^+$  emission is very patchy and several condensations are seen close to the edge of the  $^{12}\text{CO}$  outflow lobes (Figure 5c). The eastern  $\text{N}_2\text{H}^+$  condensation seems to be host G 28.87+0.07D, although the  $\text{N}_2\text{H}^+$  peak position does not agree with the mm peaks. In fact, none of the  $\text{N}_2\text{H}^+$  condensations matches the 3 mm source positions, which may indicate a low  $\text{N}_2\text{H}^+$  abundances in these cores, as suggested by Womack et al. (1992), who argue that  $\text{N}_2\text{H}^+$  is likely to be destroyed in regions of very high density ( $n_{\text{H}_2} > 10^6 \text{ cm}^{-3}$ ) and high temperature ( $T_{\text{k}} > 200 \text{ K}$ ). Alternatively, one might speculate that  $\text{N}_2\text{H}^+$  could trace the borders of a region evacuated by the outflow. However, our fit to the  $\text{N}_2\text{H}^+$  lines give LSR velocities of around  $103 \text{ km s}^{-1}$  for these condensations, namely too similar to the  $V_{\text{sys}}$  to be typical of gas participating in the outflow motion.

### 3.3.3. G 23.01–0.41

We have seen that the red wing of the  $^{12}\text{CO}$  spectrum towards G 23.01–0.41 is more prominent than the blue wing (Figure 3c). Figure 6a presents an overlay of the high velocity  $^{12}\text{CO}$  emission map on the 3 mm continuum image; Figures 6b and d, respectively, show such overlay maps for the  $^{13}\text{CO}$  and  $\text{HNCO}$  wing emissions. To obtain these maps, we integrated high velocity emission between the  $V_{\text{b}}$  and  $V_{\text{t}}$  for each wing (see §3.2 for their definitions). In order to keep a consistency in selecting velocity ranges for the 3 lines as much as possible, we integrated the blueshifted  $^{12}\text{CO}$  emission up to  $V_{\text{LSR}} = 49.9 \text{ km s}^{-1}$  beyond the  $V_{\text{t}}$ (blue) of  $64.6 \text{ km s}^{-1}$  which is the first LSR-velocity where the blueshifted wing drops below the  $1.5\sigma$  level (see Figure 3c). The resultant velocity ranges for the blueshifted gas are almost the same for the 3 tracers, while velocity interval for the  $^{12}\text{CO}$  red wing is approximately twice of those for the redshifted  $^{13}\text{CO}$  and  $\text{HNCO}$  emission.

In Figure 6a, a clear bipolar structure is seen with the bright redshifted lobe lying to the southwest and the blueshifted lobes to the northeast and southwest. In addition, a faint redshifted emission is found to the northeast of the 3 mm continuum peak. The velocity structure traced by the  $^{13}\text{CO}$  and  $\text{HNCO}$  seems to reconcile with that by the  $^{12}\text{CO}$  line in the sense that the bright blueshifted gas lies to the southwest of the 3 mm source, although the  $\text{HNCO}$  does not show blueshifted gas to the northwest. We also point out that a fainter redshifted  $\text{HNCO}$  condensation is seen to the northeast, whose position matches the northeastern  $^{12}\text{CO}$  redshifted lobe. In addition, one may notice that the redshifted gas outlined by the  $^{13}\text{CO}$  are basically same as the  $^{12}\text{CO}$ ; both the emission show their peaks to

the south of the 3 mm source and elongated towards southwest and northeast.

As in the case of G 28.87+0.07 (see §3.3.2), the above picture of the high velocity wings may be interpreted either with the existence of two distinct outflows or with the fact that the outflow axis is sufficiently close to the plane of the sky to allow the observation of both blue- and redshifted gas in each lobe. In the former hypothesis, one of the two putative (proto)stars drives the northeastern blueshifted lobe as well as the southwestern redshifted one, and the other (proto)star does the remaining two lobes. If this is the case, each (proto)star is driving a pair of outflow lobes whose masses (hence, momentum rates, see Table 7) differs significantly, which seems not to be reasonable. In conclusion, we prefer the single outflow hypothesis with the following two supporting reasons: (1) the high velocity gas maps outlined by the  $^{13}\text{CO}$  and HNC maps do not contradict with the velocity structure traced by the  $^{12}\text{CO}$ ; neither  $^{13}\text{CO}$  nor HNC maps supports the presence of two outflows, and (2) we identified only a 3 mm continuum source towards the center of the HMC (§3.1.1). We, thus, adopt the solid line in Figure 6a as the outflow axis. This line passes across the 3 mm peak position and as close as possible to the peak positions of the blue- and redshifted HNC lobes.

In Figures 6b and c we show maps of the  $^{13}\text{CO}$  and  $\text{C}^{18}\text{O}$  bulk emission integrated over a velocity range shown by the green bars in Figure 3c. These arise from a region ten times larger than the HMC traced by higher density tracers such as  $\text{CH}_3\text{CN}$ . In addition, the emission appears to peak a few arcsecond to the south of the HMC, which may be explained if the  $^{13}\text{CO}$  and  $\text{C}^{18}\text{O}$  lines are partially thick, thus hiding the densest part of the molecular cloud. To confirm this hypothesis, we have estimated the optical depth of the  $^{13}\text{CO}$  and  $\text{C}^{18}\text{O}$  gas from the ratio of the two isotopomers, assuming a relative abundance of 5.5. Note that our estimate is not affected by uncertainties due to relative calibration errors or different UV sampling, because the two lines were observed simultaneously (§2.1.1). Although the opacity estimate turns out to vary slightly across the line, depending on the velocity (from  $< 1$  to 3.4), we conclude that a mean value of  $\tau[^{13}\text{CO} (1-0)] = 2$  is appropriate for our purposes. This indicates that the optical depth of the  $^{13}\text{CO} (1-0)$  line may be sufficiently high to prevent the detection of the HMC. On the other hand,  $\text{C}^{18}\text{O}$  should be less affected by this problem. In fact a tail of  $\text{C}^{18}\text{O} (1-0)$  bulk emission is seen in Figure 6c towards the position of the HMC, although the main peak is still shifted to the south. This may be also the effect of low angular resolution, which privileges regions with larger *beam averaged* column density with respect to those (like the HMC) with enhanced volume and *source averaged* column density.

We thus obtain mean column densities of  $4.2 \times 10^{17} \text{ cm}^{-2}$  for  $^{13}\text{CO}$  and  $7.1 \times 10^{17} \text{ cm}^{-2}$  for  $\text{C}^{18}\text{O}$ , over the regions enclosed by the corresponding  $5\sigma$  contour level, which imply  $M_{\text{LTE}}$

of  $1 \times 10^4 M_\odot$  for  $^{13}\text{CO}$  and  $2 \times 10^4 M_\odot$  for  $\text{C}^{18}\text{O}$  (see Table 6). Here we assume that the same  $T_{\text{ex}}$  for both  $^{13}\text{CO}$  and  $\text{C}^{18}\text{O}$  and take it equal to the peak  $T_{\text{sb}}$  of the  $^{13}\text{CO}$  emission [ 10.3 K from Figure 3;  $T_{\text{ex}} \simeq T_{\text{sb}}^{\text{peak}}(^{13}\text{CO}) + T_{\text{bg}} = 13 \text{ K}$ ]. Despite the lack of zero-spacing information in these interferometric maps, masses like these compare well to those measured in similar objects with single-dish telescopes (e.g., G 24.78+0.08; Cesaroni et al. 2003).

Lastly, in Figure 6d we show the map of the  $\text{CH}_3\text{CN}$  emission integrated over the blue and red bars in Figure 3c. One may see that the shape of the HMC traced by this and the  $\text{NH}_3$  line (Figure 6b), as well as the 3 mm continuum (Figure 6a) is slightly elongated perpendicularly to the outflow axis. It is thus tempting to speculate that one is observing a disk-like structure rotating about that axis. We will discuss this issue in §3.6.

### 3.4. Physical Properties of the Molecular Outflows

In order to calculate the outflow properties, we used the  $^{12}\text{CO}$  wing emission maps shown in Figures 4–6. For G 28.87+0.07, where multiple outflows might be present (see §3.3.2), we consider only the most prominent lobes, as these represent the dominant contribution to the mechanical luminosity and momentum rate of the outflow system. A caveat to this approach is that the secondary outflow might be weak because heavily resolved in our interferometric maps. In other words, one cannot rule out the possibility that better UV sampling at short spacing could reveal a stronger, better defined outflow pattern. Only single-dish mapping of these regions may shed light on this issue.

The outflow parameters are calculated as follows. We integrated the outflow lobe emission encompassing the  $5\sigma$  level contours to calculate the mass of molecular hydrogen constituting the lobes ( $M_{\text{lobe}}$ ), assuming that the wing emission is optically thin. Indeed, we have estimated the optical depth in the  $^{12}\text{CO}$  line wings for G 23.01–0.41, for which  $^{13}\text{CO}$  data are available. We first reconstructed the NMA  $^{13}\text{CO}$  data with the same CLEAN beam as the PdBI  $^{12}\text{CO}$  data and then smoothed the latter to the same spectral resolution as the former. From the ratio between the  $^{12}\text{CO}$  and  $^{13}\text{CO}$  line profiles we computed the optical depth for the blue ( $47.2 \leq V_{\text{LSR}}/\text{km s}^{-1} \leq 69.0$ ) and red ( $79.9 \leq V_{\text{LSR}}/\text{km s}^{-1} \leq 96.2$ ) wings, which are respectively  $0.70 \pm 0.2$  and  $1.1 \pm 0.5$ . This indicates that the correction due to optical depth effects for the outflow mass and the relevant parameters is very small, a factor  $\sim 1.5$ . Given the similarity in the source properties, we assumed that the wing emission is optically thin also in G 16.59–0.05 and G 28.87+0.07 and used the same approach as for G 23.01–0.41.

To calculate the outflow parameters, as a lower limit for  $T_{\text{ex}}$  we adopted the maximum

$T_{\text{sb}}$  observed in all low-density tracers (CO and  $\text{HCO}^+$ ; see Figure 3), namely  $T_{\text{ex}} = 35$  K for G 16.59–0.05, 31 K for G 28.87+0.07, and 15 K for G 23.01–0.41. Subsequently we calculated the kinematical properties of the flow (see Table 7) such as the dynamical time scale ( $t_{\text{d}}$ ), mass loss rate ( $\dot{M}_{\text{flow}}$ ), and momentum rate ( $F_{\text{co}}$ ). The uncertainty on  $T_{\text{ex}}$  reflects into a 40–70% uncertainty on  $M_{\text{lobe}}$ .

One can estimate the outflow velocity from the terminal velocity of the CO spectra and the systemic velocity as  $V_{\text{flow}} = |V_{\text{t}} - V_{\text{sys}}|$ . The dynamical time scale is then given by  $l_{\text{lobe}}/V_{\text{flow}}$ , where the lobe length  $l_{\text{lobe}}$  is defined as the maximum extent of the lobe measured from the 3 mm continuum peak. In all cases  $t_{\text{d}}$  lies in the range  $(1\text{--}3)\times 10^4$  yr. Note that this estimate of  $t_{\text{d}}$  is to be taken as a lower limit because the lobe could extend beyond our field of view.

The mass loss rate,  $\dot{M}_{\text{flow}}$ , was estimated from the ratio  $M_{\text{lobe}}/t_{\text{d}}$ , and turns out to be on the order of  $10^{-4} - 10^{-3} M_{\odot} \text{ yr}^{-1}$  for all sources. Since molecular outflows appear to be momentum-driven (e.g., Cabrit & Bertout 1992) the momentum rate  $F_{\text{co}} = M_{\text{lobe}} V_{\text{flow}}^2 / l_{\text{lobe}}$  may be taken as an indicator of the strength of the outflow and hence of the mass and luminosity of the YSO powering it. The G 16.59–0.05 outflow has  $F_{\text{co}} \simeq 10^{-3} M_{\odot} \text{ km s}^{-1} \text{ yr}^{-1}$ , whereas for G 28.87+0.07 and G 23.01–0.41  $F_{\text{co}}$  are an order of magnitude higher. Values like these are typical of YSOs with luminosities of  $\sim 10^3 - 10^4 L_{\odot}$  (see Figure 5 of Richer et al. 2000 and Figure 4 of Beuther et al. 2002a), confirming that we are indeed dealing with early B (proto)stars.

These findings are not affected if one takes into account the unknown inclination angle  $i$ , here defined as the angle between the outflow axis and the line of sight. In fact,  $t_{\text{d}}$ ,  $\dot{M}_{\text{flow}}$ , and  $F_{\text{co}}$ , are proportional respectively to  $\cot i$ ,  $\tan i$ , and  $\sin i / \cos^2 i$ . Thus, assuming as extreme values  $i = 20^\circ$  and  $i = 70^\circ$ , the corrections for the three quantities above are respectively 2.7–0.36, 0.36–2.7, and 0.39–8. In conclusion, for all reasonable inclination angles, the parameters listed in Table 7 might need a correction by less than an order of magnitude, thus leaving our conclusions unaffected.

### 3.5. Temperature, Column Density and $\text{CH}_3\text{CN}$ Abundance of Cores

#### 3.5.1. Rotational Temperature and Column Density of the $\text{CH}_3\text{CN}$ Lines

Symmetric top molecules like  $\text{CH}_3\text{CN}$  are ideal probes to measure the gas kinetic temperature, because different  $K$  components belonging to the same  $J + 1 \rightarrow J$  transition are mainly excited by collisions, and spread over a few 10 MHz and can be observed simultaneously in the same bandwidth (hence, suffering less calibration errors). In addition, for



densities typical of HMCs ( $> 10^{6-7} \text{ cm}^{-3}$ ) the rotational temperature,  $T_{\text{rot}}$ , obtained from  $K$  line ratios turns out to be very close to the kinetic temperature of the  $\text{H}_2$  gas. One may thus obtain reliable estimates of the temperature and column density of the region where  $\text{CH}_3\text{CN}$  is detected through the rotation diagram method (Hollis 1982; Churchwell, Walmsley & Wood 1992).

Since optical depth effects may affect the reliability of rotation diagrams, we have attempted to fit the  $K$  components of  $\text{CH}_3\text{CN}$  with a simple LTE fit taking into account also the line opacity, as performed in e.g., Olimi et al. (1993). The results indicate that the optical depth is less than  $\sim 2$ , sufficiently low to allow usage of the rotation diagram method in our cases.

To derive mean values of  $T_{\text{rot}}$  and  $N_{\text{CH}_3\text{CN}}$  over the cores using rotation diagrams, we analyzed the mean spectra in Figure 7 obtained by averaging the emission over the regions inside  $5\sigma$  contour level of the  $K = 0+1$  emission map. Assuming that all  $K$ -components trace the same gas, we performed multiple-Gaussian fitting of the lines, forcing their widths to be identical and their separations in frequency to be equal to the laboratory values. Hence, the free parameters of the fit are the line intensities, the full width at half maximum (FWHM) of the lines, and the LSR velocity of one  $K$  component – arbitrarily chosen. Tables 8 and 9 summarize the fitting results, where  $V_{\text{sys}}$  is the best-fit LSR velocity. The line intensities were used to make rotation diagrams (see e.g. Churchwell, Walmsley & Wood 1992) from which we obtained an estimate of  $T_{\text{rot}}$  and  $N_{\text{CH}_3\text{CN}}$ . Note that our analysis is restricted to use the  $K = 0$  to 3 lines because of the limited correlator bandwidth. In these calculations, we assumed optically thin emission and adopted the partition function by Araya et al. (2005). The rotation diagrams for all three sources are presented in Figure 8, where  $N_{\text{JK}}$ ,  $E_{\text{JK}}$ , and  $g_{\text{JK}}$  represent the column density, energy, and statistical weight of level  $(J, K)$ , and  $k$  is the Boltzmann constant. In Table 9, we give the obtained values of  $T_{\text{rot}}$  and  $N_{\text{CH}_3\text{CN}}$  for the 3 HMCs.

The 3 HMCs have comparable mean  $N_{\text{CH}_3\text{CN}}$ , spanning the range  $(3-7) \times 10^{14} \text{ cm}^{-2}$  (Table 9), close to the values obtained from interferometric measurements in similar objects (e.g. G 24.78+0.08; Beltrán et al. 2005). The mean values of  $T_{\text{rot}}$  in G 16.59–0.05 and G 23.01–0.41 (120 – 130 K) are likely to be higher than that of G 28.87+0.07 (93 K), although our  $T_{\text{rot}}$  estimates have rather large errors. In G 28.87+0.07 both the temperature estimated from  $\text{NH}_3$  (see Table 9) and the  $T_{\text{sb}}$  of the  $\text{CH}_3\text{CN}$  lines ( $\sim 5 \text{ K}$  for  $K = 0 + 1$ ) are twice smaller than in the other two sources ( $\sim 10 \text{ K}$ ), suggesting that  $\text{CH}_3\text{CN}$  gas should be colder than in G 16.59–0.05 and G 23.01–0.41.

In Table 9, one may notice that the mean  $T_{\text{rot}}$  are a factor of 2 higher than the  $\text{NH}_3$  kinetic temperature ( $T_{\text{k}}$ ) derived from the VLA observations (CTC97). One possible expla-

nation for this discrepancy is that optical depth effects in the  $\text{CH}_3\text{CN}$  lines may cause an overestimate of  $T_{\text{rot}}$ . It is also worth noting that the low-energy  $\text{NH}_3$  transitions observed by CTC97 may be affected by more extended emission (and hence colder gas) than those obtained through the  $\text{CH}_3\text{CN}$  lines, as suggested in Olmi et al. (1993). In fact, these authors demonstrate that the two “thermometers”,  $\text{CH}_3\text{CN}$  and  $\text{NH}_3$ , are in reasonable agreement for  $T \lesssim 50$  K, but for higher temperature the  $T_{\text{rot}}$  estimated from  $\text{CH}_3\text{CN}$  tends to exceed that from  $\text{NH}_3$ . However, one should keep in mind that the relationship of Olmi et al. (1993) is based on single-dish observations with 6–8 times larger beam sizes than our interferometric measurements, and might hence be affected by material extended over larger regions than those imaged by us.

### 3.5.2. Fractional Abundance of $\text{CH}_3\text{CN}$ Molecules in the Cores

We have attempted an estimate of the fractional abundance of  $\text{CH}_3\text{CN}$  ( $X_{\text{CH}_3\text{CN}}$ ) from the ratio between the mean  $N_{\text{CH}_3\text{CN}}$  (Table 9) and  $\langle N(\text{H}_2) \rangle$  calculated in §3.1.2. Table 9 gives the resultant  $X_{\text{CH}_3\text{CN}}$ . We stress that the 3 mm emission from the three HMCs is dominated by thermal dust emission (§3.1.2). Note that the  $\text{CH}_3\text{CN}$  line and 3 mm continuum emission show fairly similar spatial distributions (see panels (a) and (d) in Figures 9–11). It is also worth pointing out that the errors on  $X_{\text{CH}_3\text{CN}}$  take into account only uncertainties on the flux calibration (§§2.1.1 and 2.1.2). One can see that  $X_{\text{CH}_3\text{CN}}$  lies in the range  $(0.7 - 2) \times 10^{-9}$ , marginally lower than the values quoted for the well known HMC in Orion ( $5 \times 10^{-9}$ ; see van Dishoeck et al. 1993).

## 3.6. Velocity Structure and Stability of the $\text{CH}_3\text{CN}$ Cores

Our results demonstrate that the ammonia cores imaged by CTC97 are indeed compact ( $\simeq 0.1$  pc), dense ( $\simeq 10^6 \text{ cm}^{-3}$ ), and hot ( $\simeq 100$  K) molecular cores. This strengthens the idea that high-mass (proto)stars – whose presence is suggested by the presence of  $\text{H}_2\text{O}$  and OH masers (Foster & Caswell 1989) – are embedded in such massive ( $\simeq 100 M_\odot$ ) HMCs. In the case of G 23.01–0.41, we also find evidence of a large scale clump seen in two CO isotopomers enshrouding the HMC, which is consistent with the findings of other authors (see e.g. Fontani et al. 2002 and references therein) in similar objects. In this section we wish to perform a more detailed analysis of the HMC structure by focusing on the velocity field of the gas, with the purpose of studying the HMC stability and infer the possible presence of rotation.

To gain insight into the velocity field of the gas, we used the same approach as Beltrán et al. (2004), i.e. we determined the velocity in each point of the region where CH<sub>3</sub>CN is detected, by fitting the CH<sub>3</sub>CN spectrum in such points with the method described in §3.5.1. In this way we also obtained the CH<sub>3</sub>CN line width ( $\Delta v_{\text{int}}$ ) in each point of the map: this is the FWHM after deconvolution of the instrumental resolution (Table 2). In this process, we have considered only those points for which the intensity of the  $K = 3$  line was above  $5\sigma$ . The results are shown in Table 10 and Figures 9–11. It should be also noted that the regions over which the CH<sub>3</sub>CN velocity could be determined are only barely resolved, being comparable to the synthesized beam width.

**G 16.59–0.06** The velocity field map of G 16.59–0.05 (Figure 9a) shows a gradient approximately along a line with P.A.  $\simeq 45^\circ$ , roughly perpendicular to the outflow axis. The most blueshifted gas lies at the center, while the most redshifted is seen to the northeast and southwest, close to the border of the region. A map of the line width is shown in Figure 9b and appears to have no correlation with the velocity map.

It would be surprising if the velocity gradient in this core were related to the CO outflow shown in Figure 4, because the two are inconsistent both geometrically and kinematically. On the other hand, it is difficult to believe that the CH<sub>3</sub>CN velocity is tracing rotation, since in this case the most blue- and redshifted gas should be found at the opposite extremes of the gradient. Furthermore, the velocity gradient corresponds to  $1.2 \text{ km s}^{-1}$  over 2400 AU, which implies an equilibrium mass of  $0.2 M_\odot$ , much less than the mass of the HMC.

We believe, however, that the presence of rotation about the outflow axis cannot be ruled out on the basis of our observations. In fact, the outflow appears to be close to pole-on, which would make the component along the line-of-sight of the rotation velocity very small and hence difficult to measure.

For a better understanding of the origin of the velocity gradient, one should also explain the positional displacement between the 3 mm and CH<sub>3</sub>CN peaks. We propose two hypotheses for follow-up studies:

- The continuum and CH<sub>3</sub>CN emission might arise from two distinct YSOs, the former deeply embedded in a relatively cold, massive core, the latter associated with hot gas, possibly distributed in a rotating ring, similar to those seen around binary systems in low-mass stars (e.g. GG Tau; Guilloteau et al. 1999); the lack of gas and dust at the center of the ring would explain why the continuum emission from the CH<sub>3</sub>CN peak is faint.
- If the newly formed stars lie close to the surface of the core, this might cause a peak

in the CH<sub>3</sub>CN abundance close to the stars themselves and far from the core center, where the dust column density – and hence the mm continuum emission – peaks. In this scenario, the 3 mm peak could represent a high-mass protostar, while the CH<sub>3</sub>CN peak would correspond to a relatively more evolved OB star.

**G 28.87+0.08** The velocity map of the G 28.87+0.07 core (Figure 10a) displays a clear gradient from southeast to northwest plus a less prominent one from northeast to southwest. It is worth reminding that the  $3\sigma$  contour levels of the 2.6 mm continuum (Figure 1b) and CH<sub>3</sub>CN  $K = 0 + 1$  emission (Figure 5d) are slightly elongated in a direction roughly perpendicular to the outflows (§3.3.2). Such an elongation is consistent with a flattened circumstellar toroid.

The interpretation of the isovelocity map is complicated by the fact that the number of possible outflows and their structure is unclear in this region (see §3.3.2). However, there are a few points worth of consideration:

- The velocity gradients seen in CH<sub>3</sub>CN are inconsistent with the outflow velocity – no matter whether the one- or two-outflow hypothesis is correct – because the redshifted CH<sub>3</sub>CN gas is located approximately to the E-SE of the core, whereas the redshifted CO emission is found to the W-SW.
- If a single outflow is present, its axis (solid line in Figure 10a) runs perpendicular to the most prominent CH<sub>3</sub>CN gradient.
- If instead two outflows are present, neither of these would be orthogonal to either CH<sub>3</sub>CN velocity gradient.

Assuming that the CH<sub>3</sub>CN emission is tracing a core rotating about the axis outlined by a poorly collimated CO outflow, the single outflow hypothesis in §3.3.2 seems preferable to the double outflow scenario. Additional evidence in favor of this scenario is given by the line width map of Figure 10b, which shows that significant line broadening, by  $\sim 2 \text{ km s}^{-1}$ , occurs from the core center to the border, just along the outflow axis.

The CH<sub>3</sub>CN velocity gradient corresponds to a change of  $\simeq 1.1 \text{ km s}^{-1}$  over  $\simeq 1.1 \times 10^4$  AU. If this is due to rotation, the dynamical mass ( $M_{\text{dyn}} = R_{\text{eff}} V_{\text{rot}}^2 / G$  with  $V_{\text{rot}}$  rotational velocity; Table 10) required to balance centrifugal and gravitational forces is equal to  $3 \pm 2 M_{\odot}$  (Table 10). This is an order of magnitude smaller than mass of the core estimated from 3 mm continuum flux ( $M_{\text{dust}}^{K=3} \simeq 55 M_{\odot}$ ; Table 10), over the region where the rotation velocity is measured, and two orders of magnitude less than the virial mass ( $M_{\text{vir}} \simeq R_{\text{eff}} (\Delta v_{\text{int}})^2 / G \simeq$

1100  $M_{\odot}$ ; Table 10) obtained for the same region. This fact strongly suggests that even though rotation may be present in the HMC, its contribution to gravitational equilibrium is negligible.

What does support the core against gravitational collapse? Here we should recall that the  $\Delta v_{\text{int}}$  map of Figure 10b does not show a well-defined increase of the velocity width towards the core center, as one sees, instead, in similar objects – e.g., G 31.41+0.31 and G 24.78+0.08 (Beltrán et al. 2005; see their Figures 9 and 23). Therefore, our data do not provide any evidence for infall motions towards the core center, so that infall is unlikely to contribute to line broadening. A more likely explanation for the observed line width is that of turbulent motions of the core gas, as turbulence is believed to play a dominant role on the evolution of the core and the star formation process in its interiors (e.g., McKee & Tan 2003).

**G 23.01–0.41** The G 23.01–0.41 core is significantly elongated in the southeast-northwest direction (see Figure 6d; P.A.  $\simeq 160^\circ$ ), namely perpendicular to the outflow axis, as one can see in the  $\text{NH}_3$ ,  $\text{CH}_3\text{CN}$ , and 3.3 mm continuum maps in Figure 6. In the same figure, one can appreciate that also the  $\text{C}^{18}\text{O}(1-0)$  line presents a tail of emission in the same direction, extending towards the position of the 3 mm continuum peak. All the results strongly suggest that one could be observing a flattened structure rotating about the outflow axis. To shed light on this issue, as already done for the other two sources, we plot in Figure 11a the velocity field of the  $\text{CH}_3\text{CN}$  core. Regardless of some scatter, the velocity appears to increase quite steadily along the major axis of the HMC, as expected in case of rotation about the outflow axis (denoted by the solid line in the figure). The velocity shift amounts to  $1.1 \text{ km s}^{-1}$  over  $2.6 \times 10^4 \text{ AU}$ .

Unlike the velocity, the line width increases from north-east to south-west, roughly along the outflow axis. This suggests that to some extent the  $\text{CH}_3\text{CN}$  emitting gas might also participate in the expansion. This fact could explain why the most blue- and redshifted  $\text{CH}_3\text{CN}$  emission is observed respectively to the north and south of the HMC, although the main velocity trend lies along the SE–NW direction. We conclude, that, albeit slightly affected by the outflow, the  $\text{CH}_3\text{CN}$  line emission from the HMC is mostly tracing rotation.

As already done for G 28.87+0.07, we have estimated the mass needed for rotational support of the core. This is  $M_{\text{dyn}} \simeq 8 \pm 3 M_{\odot}$ , two orders of magnitude smaller than the HMC mass  $M_{\text{dust}}^{K=3} \simeq 340 M_{\odot}$  (Table 10). Instead, the virial mass is 5 times larger than the core mass, demonstrating that as well as for G 28.87+0.07, also for G 23.01–0.41 the dominant contribution to core equilibrium is not coming from rotation but from turbulence.

### 3.7. Comparison with the Other CH<sub>3</sub>CN Cores and Future Considerations

As discussed in §3.6, we believe that we have found significant evidence of rotation in two out of three cores, while in the third object detection of rotation might be hindered by projection effects (rotation axis almost parallel to the line of sight). In any case, rotational motions are undoubtedly less prominent in these two cores than in those (G24.78+0.08 and G31.41+0.31) studied by Beltrán et al. (2004, 2005). Given the low number statistics it is impossible to draw any conclusion out of this result. However, one cannot rule out the possibility that this is an observational effect. The distance to G 23.01–0.41 is 1.4 times larger than that of G24.78 and G31.41, while the angular resolution of our observations is at least 2 times worse than that of the PdBI observations by Beltrán et al. (2004, 2005). Therefore, not only our observations are less sensitive to velocity gradients, but this makes it also more difficult to disentangle the contribution by distinct toroid-outflow systems overlapping in the same region – especially when multiple sources are present as in the case of G 28.87+0.07. In conclusion, we believe that better angular and spectral resolutions are needed to make any search for rotating disks/toroids successful.

Notwithstanding these caveats, it is worth stressing that the mere existence of rotation in two of the HMCs studied by us, albeit insufficient to guarantee support against gravitational forces, is an important clue for the process of high-mass star formation. In addition, one cannot rule out the possibility that, on smaller scales than those imaged by us, conservation of angular momentum might speed up the rotation, and thus attain centrifugal equilibrium in a circumstellar disk. This condition will be attained for radii satisfying the relation

$$R_{\text{eq}} = R_{\text{eff}} \left( \frac{M_{\text{dyn}}}{M_{\text{dust}}^{K=3}} \right)^{\frac{1}{4-p}} \quad (1)$$

whose derivation is given in Appendix A. A minimum value of  $R_{\text{eq}}$  can be obtained for  $p = 2.5$  (see e.g. Fontani et al. 2002), which gives  $R_{\text{eq}}/R_{\text{eff}} \simeq 6 \times 10^{-3}$  and  $5 \times 10^{-3}$  for G 28.87+0.07 and G 23.01–0.41, respectively. Regions like these need sub-arcsec angular resolution and a higher density tracer than CH<sub>3</sub>CN to be investigated.

## 4. Conclusions

Using the OVRO, Nobeyama, and IRAM-PdBI mm-interferometers, we carried out intensive search for rotating toroids towards the massive YSOs in G 16.59–0.05, G 28.87+0.07, and G 23.01–0.41 which exhibit no or faint free-free emission (CTC97). Our observations revealed that these objects are embedded in HMCs with masses of 95–380  $M_{\odot}$  and temperatures of 93–130 K, making the cores typical site of high-mass (proto)star formation. All the

3 objects harbored in the HMCs are driving powerful ( $F_{\text{co}} \simeq 10^{-3} - 10^{-2} M_{\odot} \text{ km s}^{-1} \text{ yr}^{-1}$ ) CO outflows. However, the nature of the outflows in G 28.87+0.07 and G 23.01–0.41 is unclear; the origin of high velocity wing emission may be attributed to either single or double outflow(s). Such ambiguity made the interpretation of velocity gradients, identified through CH<sub>3</sub>CN *K*-ladder line analysis, existing in the innermost densest part of the G 28.87+0.07 and G 23.01–0.41 HMCs fairly difficult. The velocity gradients are almost perpendicular to their molecular outflow axes, suggesting the presence of rotating, flattened structures. However, the corresponding dynamical masses are an order of magnitude smaller than the masses derived from 3 mm dust continuum emission, which indicates turbulent pressure as the dominant support of the HMCs. No conclusion could be reached for the third source, G 16.59–0.05, as the putative rotation axis appears to lie close to the line-of-sight, thus making the detection of the rotation velocity very difficult for projection effects. Further higher resolution imaging will allow us to establish the presence of rotation on a more solid ground.

The authors gratefully acknowledge the staff of OVRO, NRO, and IRAM observatories, the Spitzer Science Center, and the GILDAS software group at IRAM. This publication used archival data from the *Spitzer Space Telescope* and *MSX*. The authors thank L. Testi, R. Bachiller, and M. Tafalla for their early contribution to this study. R. S. F. acknowledges A. I. Sargent, J. M. Carpenter, H. Karoji, M. Hayashi, and S. S. Hayashi for their continuous encouragement and support, T. Y. Brooke for his generous help with data reduction of the GLIMPSE images. During this work, M. T. B. was supported by MEC grant AYA2005-08523-C0, and R.S.F. was supported by OVRO mm-array postdoctoral fellowship program under NSF grant AST 02-28955.

## A. Centrifugal Radius

Here we calculate an expression of the radius at which centrifugal equilibrium can be attained inside a rotating, spherically symmetric core. The hypothesis is that the rotation velocity  $V_{\text{rot}}$  observed at radius  $R_{\text{eff}}$  is not sufficient to sustain the core against gravitational forces thus allowing contraction and speed up of the gas in the core until centrifugal equilibrium is attained. If this occurs at radius  $R_{\text{eq}}$  with velocity  $V_{\text{eq}}$ , conservation of angular momentum per unit mass gives the following relation:

$$V_{\text{eq}} R_{\text{eq}} = V_{\text{rot}} R_{\text{eff}} \quad (\text{A1})$$

while the equilibrium condition turns into

$$V_{\text{eq}}^2 = \frac{G M(R_{\text{eq}})}{R_{\text{eq}}}. \quad (\text{A2})$$

The mass  $M(R)$  contained inside radius  $R$  depends on the dependence of the gas volume density  $n$  on the radius. Assuming that  $n$  varies with  $R^{-p}$ , one obtains  $M(R) \propto R^{3-p}$ . Therefore, we can write the following relation

$$M(R_{\text{eq}}) = M(R_{\text{eff}}) \left( \frac{R_{\text{eq}}}{R_{\text{eff}}} \right)^{3-p} \quad (\text{A3})$$

where  $M(R_{\text{eff}}) = M_{\text{dust}}^{K=3}$  measured by us from the mm continuum emission.

Substituting  $V_{\text{eq}}$  from Eq. (A1) and  $M(R_{\text{eq}})$  from Eq. (A3) into Eq. (A2), and replacing  $V_{\text{rot}}$  with  $M_{\text{dyn}}$  from the definition, we find

$$M_{\text{dyn}} = \frac{R_{\text{eff}} V_{\text{rot}}^2}{G}, \quad (\text{A4})$$

one consequently obtains the expression of  $R_{\text{eq}}$  as a function of measurable quantities:

$$R_{\text{eq}} = R_{\text{eff}} \left( \frac{M_{\text{dyn}}}{M_{\text{dust}}^{K=3}} \right)^{\frac{1}{4-p}}. \quad (\text{A5})$$

## REFERENCES

- Araya, E., Hofner, P., Kurtz, S., Bronfman, L., & DeDeo, S. 2005, *ApJS*, 157, 279
- Bally, J., & Zinnecker, H. 2005, *AJ*, 129, 2281
- Behrend, R., & Maeder, A. 2001, *A&A*, 373, 190
- Beltrán, M. T., Cesaroni, R., Neri, R., Codella, C., Furuya, R. S., Testi, L., & Olmi, L. 2004, *ApJ*, 601, L187
- Beltrán, M. T., Cesaroni, R., Neri, R., Codella, C., Furuya, R. S., Testi, L., & Olmi, L. 2005, *A&A*, 435, 901
- Beltrán, M. T., Cesaroni, R., Codella, C., Testi, L., Furuya, R. S., & Olmi, L. 2006, *Nature*, 443, 427
- Benjamin, R. A., et al. 2003, *PASP*, 115, 953



- Benson, P. J., Caselli, P., & Myers, P. C. 1998, *ApJ*, 506, 743
- Beuther, H., Schilke, P., Sridharan, T. K., Menten, K. M., Walmsley, C. M., & Wyrowski, F. 2002a, *A&A*, 383, 892
- Beuther, H., Schilke, P., Gueth, F., McCaughrean, M., Andersen, M., Sridharan, T. K., and Menten, K. M., 2002b, *A&A* 387, 931
- Beuther, H., Schilke, P., and Stanke, T., 2003, *A&A* 408, 601
- Beuther, H., Schilke, P., and Gueth, F., 2004, *ApJ* 608, 330
- Beuther, H., Zhang, Q., Bergin, E. A., Sridharan, T. K., Hunter, T. R., & Leurini, S. 2007, *A&A*, 468, 1045
- Bonnell, I. A., Bate, M. R., & Zinnecker, H. 1998, *MNRAS*, 298, 93
- Bonnell, I. A., & Bate, M. R. 2002, *MNRAS*, 336, 659
- Bonnell, I. A., Vine, S. G. & Bate, M. R. 2004, *MNRAS*, 349, 735
- Burrows, C. J., et al. 1996, *ApJ*, 473, 437
- Cabrit, S. & Bertout, C. 1992, *A&A*, 261, 274
- Caselli, P., Benson, P. J., Myers, P. C., & Tafalla, M. 2002, *ApJ*, 572, 238
- Cesaroni, R., Hofner, P., Walmsley, C.M., & Churchwell, E. 1998, *A&A*, 331, 709
- Cesaroni, R., Codella, C., Furuya, R. S., & Testi, L. 2003, *A&A*, 401, 227
- Cesaroni, R., Neri, R., Olmi, L., Testi, L., Walmsley, C. M., & Hofner, P. 2005, *A&A*, 434, 1039
- Cesaroni, R., Galli, D., Lodato, G., Walmsley, C. M., & Zhang, Q. 2007, *Protostars and Planets V*, 197
- Churchwell, E., Walmsley, C. M., & Wood, D.O.S. 1992, *A&A*, 253, 541
- Codella, C., Testi, L., & Cesaroni, R. 1997, *A&A*, 325, 282 (CTC97)
- Crutcher, R. M. 1999, *ApJ*, 520, 706
- Fontani, F., Cesaroni, R., Caselli, P., & Olmi, L. 2002, *A&A*, 389, 603
- Fontani, F., et al. 2004a, *A&A*, 414, 299

- Fontani, F., et al. 2004b, *A&A*, 424, 179
- Forster, J. R., & Caswell, J. L. 1989, *A&A*, 213, 339
- Furuya, R. S., Cesaroni, R., Codella, C., Testi, L., Bachiller, R., & Tafalla, M. 2002, *A&A*, 390, L1
- Furuya, R. S., Cesaroni, R., Takahashi, S., Momose, M., Testi, L., Shinnaga, H., & Codella, C. 2005, *ApJ*, 624, 827
- Furuya, R. S., Kitamura, Y., & Shinnaga, H. 2006, *ApJ*, 653, 1369
- Guilloteau, S., Dutrey, A., & Simon, M. 1999, *a*, 348, 570
- Hildebrand, R. H. 1983, *QJRAS*, 24, 267
- Hollis, J. M. 1982, *ApJ*, 260, 159
- Kruegel, E., & Walmsley, C. M. 1984, *A&A*, 130, 5
- Kurtz, S., Cesaroni, R., Churchwell, E., Hofner, P., & Walmsley, C. M. 2000, in *Protostars and Planets IV*, ed. V. Mannings, A. Boss, & S. Russell (Tucson: Univ. Arizona Press), 299
- Loren, R. B., & Mundy, L. G. 1984, *ApJ*, 286, 232
- Maxia, C., Testi, L., Cesaroni, R., & Walmsley, C. M. 2001, *A&A*, 371, 287
- McKee, C. F., & Tan, J. C. 2003, *ApJ*, 585, 850
- Molinari, S., Testi, L., Brand, J., Cesaroni, R., & Palla, F. 1998, *ApJ*, 505, L39
- Molinari, S., Brand, J., Cesaroni, R., & Palla, F. 2000, *A&A*, 355, 617
- Olmi, L., Cesaroni, R., & Walmsley, C. M. 1993, *A&A*, 276, 489
- Olmi, L., Cesaroni, R., Hofner, P., Kurtz, S., Churchwell, E., & Walmsley, C. M. 2003, *A&A*, 407, 225
- Palla, F., & Stahler, S. W. 1993, *ApJ*, 418, 414
- Preibisch, T., Ossenkopf, V., Yorke, H. W., & Henning, T. 1993, *A&A*, 279, 577
- Price, S. D., Egan, M. P., Carey, S. J., Mizuno, D. R., & Kuchar, T. A. 2001, *AJ*, 121, 2819

- Richer, J. S., Shepherd, D. S., Cabrit, S., Bachiller, R., & Churchwell, E. 2000, *Protostars and Planets IV*, 867
- Scoville, N. Z., Sargent, A. I., Sanders, D. B., Claussen, M. J., Masson, C. R., Lo, K. Y., & Phillips, T. G. 1986, *ApJ*, 303, 416
- Simon, M., Dutrey, A., & Guilloteau, S. 2000, *ApJ*, 545, 1034
- van Dishoeck, E. F., Blake, G. A., Draine, B. T., & Lunine, J. I. 1993, in *Protostars and Planets III*, ed. E. H. Levy and J.I. Lunine (Tucson: Univ. Arizona Press), 163
- Yorke, H. W., & Sonnhalter, C. 2002, *ApJ*, 569, 846
- Whitney, B. A., et al. 2004, *ApJS*, 154, 315
- Womack, M., Ziurys, L. M., & Wyckoff, S. 1992, *ApJ*, 387, 417

Table 1. Summary of Interferometric Continuum Emission Observations

Source	Telescope	Frequency (GHz)	Bandwidth <sup>a</sup> (GHz)	Synthesized Beam		Image RMS (mJy beam <sup>-1</sup> )
				$\theta_{\text{maj}} \times \theta_{\text{min}}$ (arcsec)	P.A. (deg)	
G 16.59–0.05	OVRO	92.0 <sup>b</sup>	3.5	$2.31 \times 1.75$	–24	0.50
	IRAM	115.3	0.32	$6.31 \times 4.10$	–167	2.49
G 28.87+0.07	OVRO	92.0 <sup>b</sup>	3.5	$2.10 \times 1.80$	–74	0.51
	IRAM	115.3	0.32	$4.97 \times 4.15$	+23	1.59
G 23.01–0.41	NMA	98.8 <sup>c</sup>	1.0	$2.69 \times 1.93$	–14	0.99
	NMA	110.0 <sup>c</sup>	1.0	$2.40 \times 1.69$	–12	1.35
	IRAM	115.3	3.5	$5.50 \times 4.17$	–164	1.90

<sup>a</sup>Effective bandwidth of line-free channels for obtaining continuum image.

<sup>b</sup>Center frequency of both the side bands.

<sup>c</sup>Center frequency of each single side band.

Table 2. Summary of Interferometric Molecular Line Observations

Source	Line	Tracking Frequency (MHz)	Telescope	Velocity Resolution (km s <sup>-1</sup> )	Synthesized Beam		Image <sup>a</sup> RMS (mJy beam <sup>-1</sup> )
					$\theta_{\text{maj}} \times \theta_{\text{min}}$ (arcsec)	P.A. (deg)	
G 16.59–0.05	HCO <sup>+</sup> (1–0)	89188.518	OVRO	1.68	$3.26 \times 1.95$	–10	51
	CH <sub>3</sub> CN (5–4)	90584.244	OVRO	1.63	$2.46 \times 1.96$	–27	18
	N <sub>2</sub> H <sup>+</sup> (1–0)	93173.900	OVRO	0.80	$2.45 \times 1.85$	–46	27
	<sup>12</sup> CO (1–0)	115271.204	IRAM	1.63	$6.31 \times 4.10$	–167	43
G 28.87+0.07	HCO <sup>+</sup> (1–0)	89188.518	OVRO	1.68	$3.51 \times 2.33$	–9	23
	CH <sub>3</sub> CN (5–4)	90584.244	OVRO	1.63	$2.47 \times 2.05$	–61	18
	N <sub>2</sub> H <sup>+</sup> (1–0)	93173.900	OVRO	0.80	$2.33 \times 1.58$	–71	28
	<sup>12</sup> CO (1–0)	115271.204	IRAM	1.63	$4.58 \times 4.58$	–21	24
G 23.01–0.41	C <sup>18</sup> O (1–0)	109782.156	NMA	5.44	$7.44 \times 5.52^c$	–21	25
	HNCO 5 <sub>05</sub> – 4 <sub>04</sub>	109905.753	NMA	5.44	$7.44 \times 5.52^c$	–21	27
	CH <sub>3</sub> CN (6–5)	109997.353	NMA	0.34 <sup>b</sup>	$2.86 \times 1.67$	–9	43
	<sup>13</sup> CO (1–0)	110201.352	NMA	5.44	$7.44 \times 5.52^c$	–21	32
	<sup>12</sup> CO (1–0)	115271.204	IRAM	0.41	$5.50 \times 4.17$	–165	43

<sup>a</sup>Typical Image noise level with the velocity resolution shown in the column 5.

<sup>b</sup>Effective resolution after smoothing.

<sup>c</sup>Received with the same intermediate-frequency, leading to the identical beam size for the lines.

Table 3. Properties of 3 mm Continuum Emission

Source	$d^a$ (kpc)	$\nu$ (GHz)	Peak Position		$R_{\text{eff}}^b$ (pc)	$S_\nu^c$ (mJy)
			R.A.(J2000)	Dec.(J2000)		
G 16.59–0.05	4.7	92.0	18:21:09.06	–14:31:47.9	0.033	37.5±7.5
		115.3	18:21:09.06	–14:31:47.5	0.055	79.6±16
G 28.87+0.07	7.4	92.0	18:43:46.25	–03:35:29.9	0.029	11.3±2.3
		115.3	18:43:46.31	–03:35:29.2	0.102	42.6±8
G 28.87+0.07B		92.0	18:43:46.19	–03:35:12.9	0.033	1.7±0.3
G 28.87+0.07C		92.0	18:43:46.31	–03:35:15.4	~ 0.01	1.5±0.4
G 28.87+0.07D		115.3	18:43:47.09	–03:35:32.0	0.030 <sup>d</sup>	0.80±0.2
G 23.01–0.41	10.7	98.8	18:34:40.29	–09:00:38.1	0.068	27.8±5.6
		110.0	18:34:40.29	–09:00:38.6	0.055	31.6±6.3
		115.3	18:34:40.30	–09:00:38.2	0.103	33.9±6.8

Note. — See Table 1 for the parameters of observations and §3.1.1 for the adopted detection criteria.

<sup>a</sup>Distance to the region, see §2 of CTC97.

<sup>b</sup>Effective radius, see §3.1.1 for the definition.

<sup>c</sup>Total flux density integrated over the region enclosed by the  $5\sigma$  level contour.

<sup>d</sup> $\sqrt{A/\pi}$  for the area encompassed by the  $5\sigma$  contour is given because the area is smaller than the beam size (Table 1).

Table 4. Flux Densities of the 3 HMCs at Infrared Wavelengths

Source	21.3 $\mu\text{m}$		14.7 $\mu\text{m}$		12.1 $\mu\text{m}$		8.3 $\mu\text{m}$		8.0 $\mu\text{m}$		5.8 $\mu\text{m}$		4.5 $\mu\text{m}$		3.6 $\mu\text{m}$	
	$S$ (Jy)	Note	$S$ (Jy)	Note	$S$ (Jy)	Note	$S$ (Jy)	Note	$S$ (Jy)	Note	$S$ (Jy)	Note	$S$ (Jy)	Note	$S$ (Jy)	Note
G 16.59−0.05	7.7	1,2	1.8	1,2	4.1	1,2,3	2.4	1,2	6.8E−2	2,4	3.3E−2	2,4	1.4E−2	2,4	...	5
G 28.87+0.07	14.7	1,2	6.8	1,2	5.1	1,2	2.8	1,2	1.3	2,4	8.0E−1	2,4	4.0E−1	2,4	6.0E−2	2,4
G 23.01−0.41	4.4	1,2	< 0.51	1,6	< 0.86	1,6	< 0.20	1,6	1.1E−1	2,4	1.1E−1	2,4	6.3E−2	2,4	1.0E−2	2,4

Note. — 1: MSX data, 2: integrated inside the 50% level contour of the data, 3: contaminated with the nearby source(s), 4: GLIMPSE data, 5: impossible to define a point source (see Figure 1, and 6:  $3\sigma$  upper limit. See §3.1.2 for the details.

Table 5. Core Mass Estimated from 3 mm Continuum Emission

Source	$M_{\text{dust}}^{\text{a}}$ ( $M_{\odot}$ )	$\langle N(\text{H}_2) \rangle^{\text{b}}$ ( $\times 10^{23} \text{ cm}^{-2}$ )
G 16.59–0.05	$95 \pm 6$	$3.0 \pm 0.9$
G 28.87+0.07	$100 \pm 7$	$4.2 \pm 1.3$
G 23.01–0.41	$380 \pm 22$	$3.6 \pm 1.1$

Note. — See §3.1.2 for the details.

<sup>a</sup>Mass of the core estimated from the 3 mm continuum flux density shown in Table 3. We assumed that  $T_{\text{dust}}$  is equal to  $T_{\text{rot}}$  of  $\text{CH}_3\text{CN}$  emission (Table 9).

<sup>b</sup>Mean  $\text{H}_2$  column density calculated over the area encompassing the emission inside the  $5\sigma$  contour.

Table 6. Properties of the Large-Scale Clumps Surrounding the 3 HMCs

Source	Probe	$R_{\text{eff}}^{\text{a}}$ (pc)	$M_{\text{LTE}}^{\text{b}}$ ( $M_{\odot}$ )
G 16.59–0.05	$\text{HCO}^+ (1-0)$	0.070	440 – 1500
	$\text{N}_2\text{H}^+ (1-0)$	0.15	540
G 28.87+0.07	$\text{HCO}^+ (1-0)$	0.12	84 – 360
G 23.01–0.41	$^{13}\text{CO} (1-0)$	0.426	$1 \times 10^4$
	$\text{C}^{18}\text{O} (1-0)$	0.174	$2 \times 10^4$

Note. — For details, see §3.3.

<sup>a</sup>Effective radius, see §3.1.1 for the definition.

<sup>b</sup>LTE-mass obtained by integrated the emission over the area enclosed by the  $5\sigma$  level contours.



Table 7. Parameters of Molecular Outflows

Source	Lobe	$M_{\text{lobe}}^{\text{a}}$ ( $M_{\odot}$ )	$t_{\text{d}}^{\text{b}}$ (yrs)	$\dot{M}_{\text{flow}}^{\text{c}}$ ( $M_{\odot} \text{ yr}^{-1}$ )	$F_{\text{CO}}^{\text{d}}$ ( $M_{\odot} \text{ km s}^{-1} \text{ yr}^{-1}$ )
G 16.59–0.05	Blue	21±11	$2.7 \times 10^4$	$(2 \pm 1) \times 10^{-4}$	$(9 \pm 5) \times 10^{-3}$
	Red	7±4	$1.4 \times 10^4$	$(5 \pm 3) \times 10^{-4}$	$(9 \pm 5) \times 10^{-3}$
G 28.87+0.07	Blue	25±12	$2.6 \times 10^4$	$(3 \pm 2) \times 10^{-4}$	$(2 \pm 1) \times 10^{-2}$
	Red	90±40	$3.1 \times 10^4$	$(2 \pm 1) \times 10^{-3}$	$(5 \pm 3) \times 10^{-2}$
G 23.01–0.41	Blue SW	17±12	$2.5 \times 10^4$	$(9 \pm 7) \times 10^{-4}$	$(2.5 \pm 1.5) \times 10^{-2}$
	Blue NE	14±10	$2.8 \times 10^4$	$(6 \pm 3) \times 10^{-4}$	$(1.9 \pm 1.2) \times 10^{-2}$
	Red SW	140±70	$3.4 \times 10^4$	$(4 \pm 3) \times 10^{-3}$	$(1.3 \pm 0.7) \times 10^{-1}$
	Red NE	4±3	$3.4 \times 10^4$	$(1.2 \pm 0.7) \times 10^{-4}$	$(3.5 \pm 3.0) \times 10^{-3}$

Note. — Outflow characteristic estimated from the  $^{12}\text{CO}$  (1–0) data, see §3.4. All the errors are considered only for the  $T_{\text{ex}}$  uncertainty.

<sup>a</sup>Outflow lobe mass.

<sup>b</sup>Dynamical time scale.

<sup>c</sup>Outflow mass loss rate.

<sup>d</sup>Outflow momentum flux.

Table 8. Results of  $\text{CH}_3\text{CN}$  Spectra Analysis

Source	Transition	$V_{\text{LSR}}^{\text{a}}$ ( $\text{km s}^{-1}$ )	$\Delta v^{\text{b}}$ ( $\text{km s}^{-1}$ )	$\int T_{\text{sb}} dv$ ( $\text{K} \cdot \text{km s}^{-1}$ )			
				$K = 0$	1	2	3
G 16.59–0.05	$J = 5-4$	59.9±0.2	5.6±0.2	20.5±1.2	14.1±1.2	10.5±1.1	13.7±1.1
G 28.87+0.07	$J = 5-4$	103.5±0.3	9.1±0.4	12.9±1.4	11.5±1.5	7.8±0.9	7.7±0.9
G 23.01–0.41	$J = 6-5$	77.4±0.1	8.3±0.2	16.2±0.8	16.7±0.8	15.0±0.6	13.8±0.6

Note. — For details, see §3.5.1.

<sup>a</sup>Centroid velocity from the multiple-Gaussian profile fitting. We adopted the  $V_{\text{LSR}}$  in column 3 as the  $V_{\text{sys}}$  of the HMCs.

<sup>b</sup>Line width in FWHM.

Table 9. Summary of Methyl Cyanide RD Analysis

Source	$R_{\text{eff}}^{\text{a}}$ (pc)	Temperature <sup>b</sup> (K)		$N_{\text{CH}_3\text{CN}}^{\text{c}}$ ( $\text{cm}^{-2}$ )	$X_{\text{CH}_3\text{CN}}^{\text{d}}$ ( $\times 10^{-10}$ )
		$T_{\text{rot}}(\text{CH}_3\text{CN})$	$T_{\text{k}}(\text{NH}_3)$		
G 16.59–0.05	0.029	$130^{+36}_{-23}$	54	$(6.9^{+2.9}_{-1.5}) \times 10^{14}$	$20 \pm 7$
G 28.87+0.07	0.042	$93^{+31}_{-18}$	37	$(3.1^{+1.3}_{-0.6}) \times 10^{14}$	$7 \pm 2$
G 23.01–0.41	0.065	$121^{+17}_{-13}$	58	$(4.6^{+0.9}_{-0.5}) \times 10^{14}$	$13 \pm 4$

Note. — For details, see §§3.5.1 and 3.5.2.

<sup>a</sup>Effective radius for the  $\text{CH}_3\text{CN}$   $K = 0 + 1$  emitting region, see §3.1.1 for the definition.

<sup>b</sup>Rotational temperature for  $\text{CH}_3\text{CN}$  (§3.5.1) and kinetic temperature for  $\text{NH}_3$  (CTC97).

<sup>c</sup>Total column density of  $\text{CH}_3\text{CN}$ .

<sup>d</sup>Fractional abundance of  $\text{CH}_3\text{CN}$  obtained from comparisons with the mean  $\langle N(\text{H}_2) \rangle$  in Table 5.

Table 10. Properties of the Central Regions of the 3 HMCs

Source	$M_{\text{dust}}^{\text{a}}$ ( $M_{\odot}$ )	$\Delta v_{\text{int}}^{\text{b}}$ ( $\text{km s}^{-1}$ )	$M_{\text{vir}}^{\text{c}}$ ( $M_{\odot}$ )	$V_{\text{rot}}^{\text{d}}$ ( $\text{km s}^{-1}$ )	$M_{\text{dyn}}^{\text{e}}$ ( $M_{\odot}$ )	$M_{\text{dust}}^{K=3, \text{f}}$ ( $M_{\odot}$ )
G 16.59–0.05	$95 \pm 6$	$5.4 \pm 0.3$	$180 \pm 15$	...	...	...
G 28.87+0.07	$100 \pm 7$	$9.1 \pm 0.4$	$780 \pm 78$	$\simeq 0.5$	$3 \pm 2$	$55 \pm 3$
G 23.01–0.41	$380 \pm 22$	$8.6 \pm 0.2$	$1100 \pm 40$	$\simeq 0.6$	$8 \pm 3$	$340 \pm 20$

Note. — For details, see §3.6.

<sup>a</sup>From Table 5.

<sup>b</sup>Intrinsic velocity width ( $\Delta v_{\text{int}}$ ) in FWHM after deconvolving the instrumental velocity resolution (Table 2) where  $\Delta v_{\text{int}}$  is measured over the region enclosed by the 50% level contour of the emission. Here, contributions of thermal gas motions are 0.38, 0.32, and  $0.37 \text{ km s}^{-1}$  for G 16.59–0.05, G 28.87+0.07, and G 23.01–0.41, respectively, when we assume that kinematical temperature ( $T_{\text{k}}$ ) of the gas is equal to the mean  $T_{\text{rot}}$  in Table 9.

<sup>c</sup>Virial mass over the 50% area of  $\text{CH}_3\text{CN}$   $K = 0 + 1$  emission. We adopted  $R_{\text{eff}}$  in Table 9 for calculating  $M_{\text{vir}}$ .

<sup>d</sup>Rotation velocity assuming that the velocity gradient is produced by rotation of the core.

<sup>e</sup>Dynamical mass.

<sup>f</sup>Core mass calculated from the 3 mm continuum flux density over the region enclosed by the  $5\sigma$  level contour of the  $\text{CH}_3\text{CN}$   $K = 3$  emission.

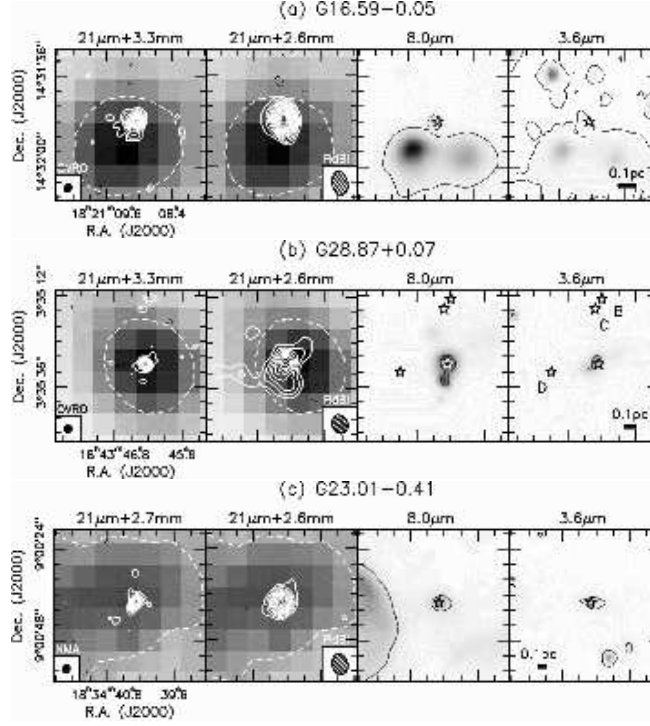


Fig. 1.— Continuum emission maps towards the 3 HMCs at mm- and infrared wavelengths. The left two panels for each source shows an overlay of mm-contour emission (white contours) on the 21  $\mu\text{m}$  one from the MSX satellite data base; the single white dashed contour indicates the 50% level of the 21  $\mu\text{m}$  emission. The ellipses in the inserted panels show the HPBW of the synthesized beam (Table 1). The right two panels show 8.0 and 3.6  $\mu\text{m}$  images from the Spitzer GLIMPSE survey; the stars mark the peak positions of the mm continuum source, and the thin contour indicate the 50% level contour of the peak intensity of the main cores of our interests. Contours for the mm-contour maps are  $2\sigma$  intervals, starting from the  $3\sigma$  level (see Table 1 for the RMS noise levels). In the panel (b), the associated labels indicate names of the mm sources identified by us (see §3.1.1 and Table 3).

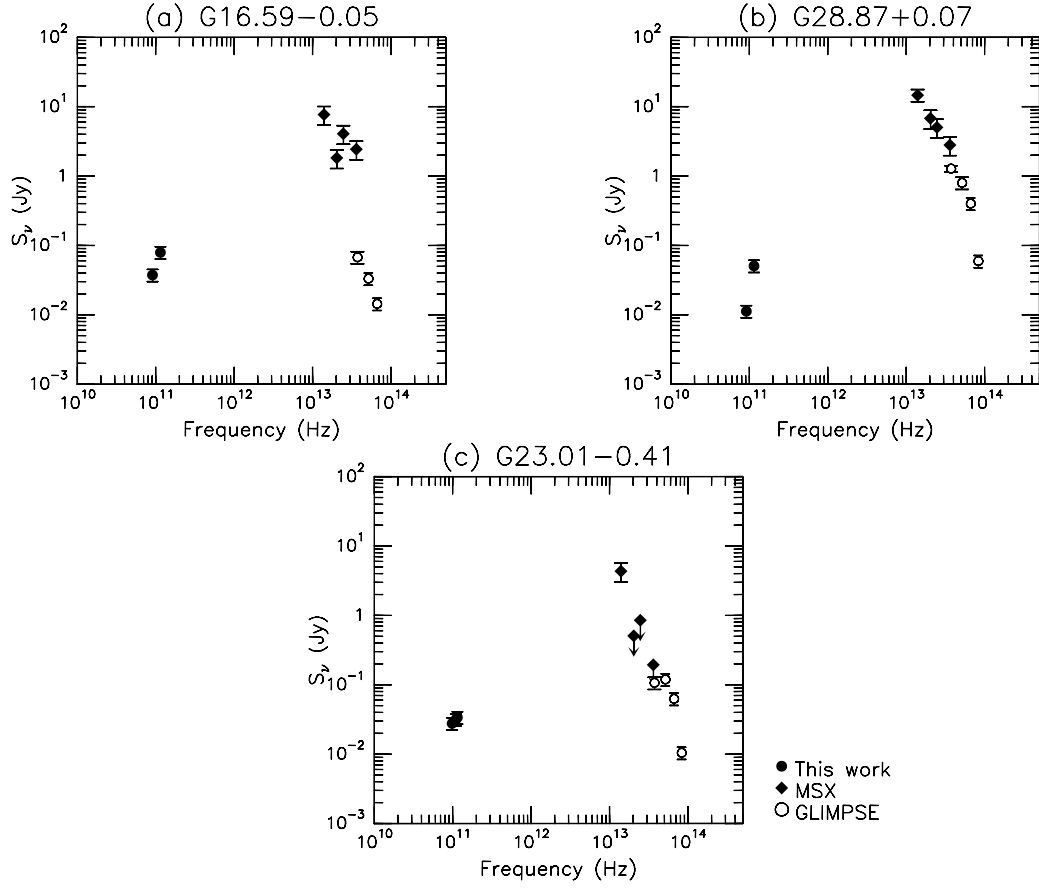


Fig. 2.— Continuum spectra of the 3 HMCs. The flux densities at 3 mm and infrared bands are summarized in Tables 3 and 4, respectively.

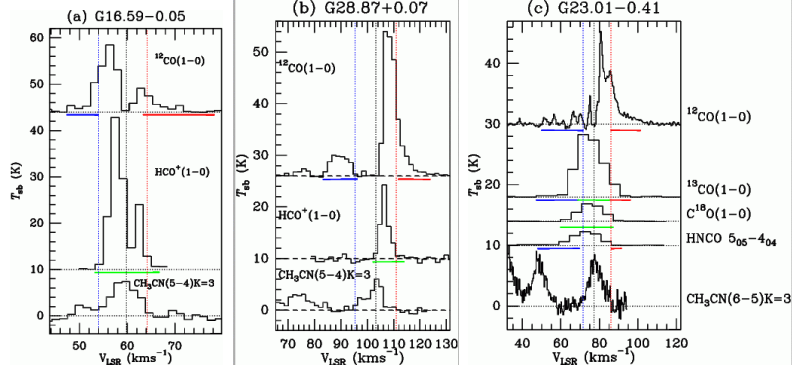


Fig. 3.— Interferometric molecular line spectra towards the peak positions of each emission in  $T_{\text{sb}}$  scale. The black vertical dashed lines indicate the  $V_{\text{sys}}$  obtained from the  $\text{CH}_3\text{CN}$  line analysis (Table 8):  $V_{\text{LSR}} = 59.8 \text{ km s}^{-1}$  for G 16.59–0.05,  $103.3 \text{ km s}^{-1}$  for G 28.87+0.07, and  $77.3 \text{ km s}^{-1}$  for G 23.01–0.41. The vertical blue and red dashed lines throughout the panels show the boundary velocities ( $V_b$ ; see §3.3.1 for the definitions) between the core gas and the blue- or redshifted outflow lobes, respectively. The blue, green, and red bars under the spectra indicate velocity ranges to obtain integrated intensity maps shown in Figures 4 – 6. The  $\text{CH}_3\text{CN}$  emission seen in  $V_{\text{LSR}} \lesssim 60 \text{ km s}^{-1}$  at G 23.01–0.41 is the other  $K$ -components (see Figure 7).

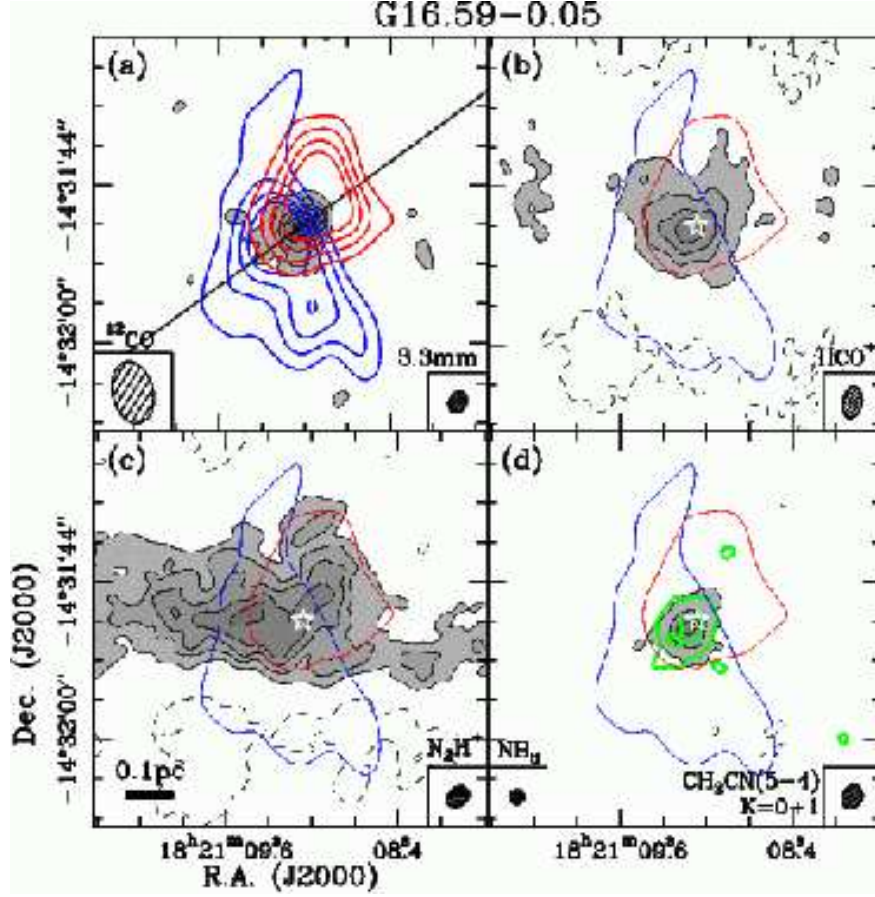


Fig. 4.— Maps of molecular lines and continuum emission for G 16.59–0.05. (a) Overlays of the blue- and redshifted wing emission maps of  $^{12}\text{CO}$  (1–0) on the 3 mm continuum emission (grey scale), total integrated intensity maps of (b)  $\text{HCO}^+$  (1–0) and (c)  $\text{N}_2\text{H}^+$  (1–0) emission (grey scale plus contour), and (d) overlay of total maps of  $\text{NH}_3$  (3,3) (green contours; CTC97) on  $\text{CH}_3\text{CN}$   $K = 0$  and 1 line emission (grey scale). In the panels (b)–(d), the thin blue- and red contours indicate the  $5\sigma$  levels of the blue- and redshifted  $^{12}\text{CO}$  (1–0) lobes shown in (a). All the contours, except for the  $^{12}\text{CO}$ , start from the  $3\sigma$  level with a  $3\sigma$  step. The dashed contours correspond to  $-3\sigma$  and  $-6\sigma$  levels for  $\text{HCO}^+$  in panel (b),  $\text{N}_2\text{H}^+$  in (c), and  $\text{CH}_3\text{CN}$  in (d). Contours for the  $^{12}\text{CO}$  outflow maps are drawn with  $5\sigma$ ,  $10\sigma$ ,  $15\sigma$ ,  $20\sigma$ , and  $40\sigma$  levels for the clarity of the plots. The RMS noise levels of the images are 33, 19, 0.50, 0.43, 0.10, 4.2, and 0.26 mJy beam $^{-1}$  for  $^{12}\text{CO}$  blueshifted,  $^{12}\text{CO}$  redshifted, 3 mm continuum,  $\text{HCO}^+$ ,  $\text{N}_2\text{H}^+$ ,  $\text{NH}_3$ , and  $\text{CH}_3\text{CN}$  maps, respectively. The solid lines in (a) indicate the identified outflow axes (§3.3.1). The central star in (b)–(d) marks the peak position of the 3 mm continuum emission. The blue and redshifted  $^{12}\text{CO}$  (1–0) emission is integrated over the velocity ranges of  $47.4 \leq V_{\text{LSR}}/\text{km s}^{-1} \leq 54.0$  and  $63.4 \leq V_{\text{LSR}}/\text{km s}^{-1} \leq 78.1$ , respectively. The  $\text{HCO}^+$  (1–0) line is integrated over  $53.3 \leq V_{\text{LSR}}/\text{km s}^{-1} \leq 66.7$ . These velocity ranges are shown by the horizontal color bars under the spectra shown in Figure 3a. For the  $\text{N}_2\text{H}^+$  (1–0) emission, all the hyperfine emission detected in  $49.4 \leq V_{\text{LSR}}/\text{km s}^{-1} \leq 70.6$  is integrated. The frequency range to obtain the  $\text{CH}_3\text{CN}$   $K = 0 + 1$  map is shown by a horizontal bar under the corresponding spectrum in Figure 7. The ellipse at the lower corners in each panel shows the synthesized beam size (Tables 1 and 2).

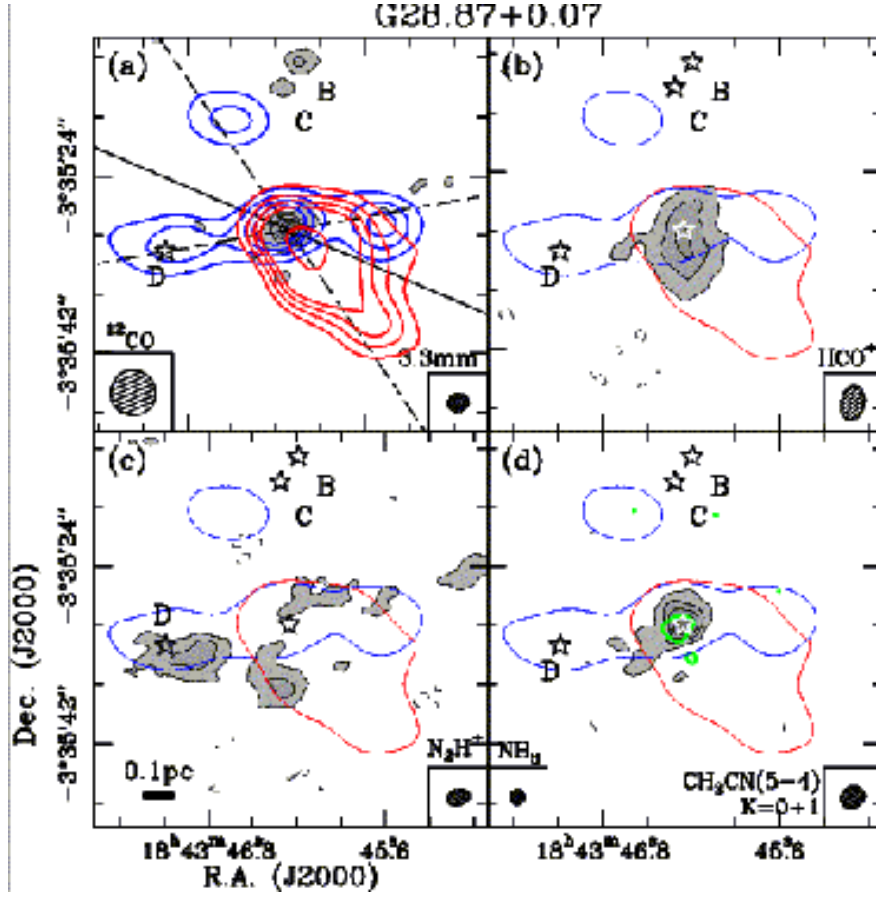


Fig. 5.— Maps of molecular lines and continuum emission for G28.87+0.07. All the contours and symbols are the same as those in Figure 4. The RMS noise levels of the images are 47, 24, 0.51, 0.3, 0.13, 5.0, and 0.18 for  $^{12}\text{CO}$  blueshifted,  $^{12}\text{CO}$  redshifted, 3mm continuum,  $\text{HCO}^+$ ,  $\text{N}_2\text{H}^+$ ,  $\text{NH}_3$  (CTC97), and  $\text{CH}_3\text{CN}$  maps, respectively. The dashed contours correspond to the  $-3\sigma$  level for  $\text{HCO}^+$  in panel (b),  $\text{N}_2\text{H}^+$  in (c), and  $\text{CH}_3\text{CN}$  in (d). The blue and redshifted  $^{12}\text{CO}$  (1–0) emission,  $\text{HCO}^+$ , and  $\text{N}_2\text{H}^+$  are integrated over the velocity ranges of  $83.3 \leq V_{\text{LSR}}/\text{km s}^{-1} \leq 96.3$ ,  $111.8 \leq V_{\text{LSR}}/\text{km s}^{-1} \leq 123.9$ ,  $102.3 \leq V_{\text{LSR}}/\text{km s}^{-1} \leq 114.0$ , and  $95.0 \leq V_{\text{LSR}}/\text{km s}^{-1} \leq 111.1$ , respectively (see also Figure 3b). The star with the associated labels indicate the peak positions and names of the mm sources identified by us (see §3.1.1 and Table 3). All the other symbols are the same as in Figure 4.

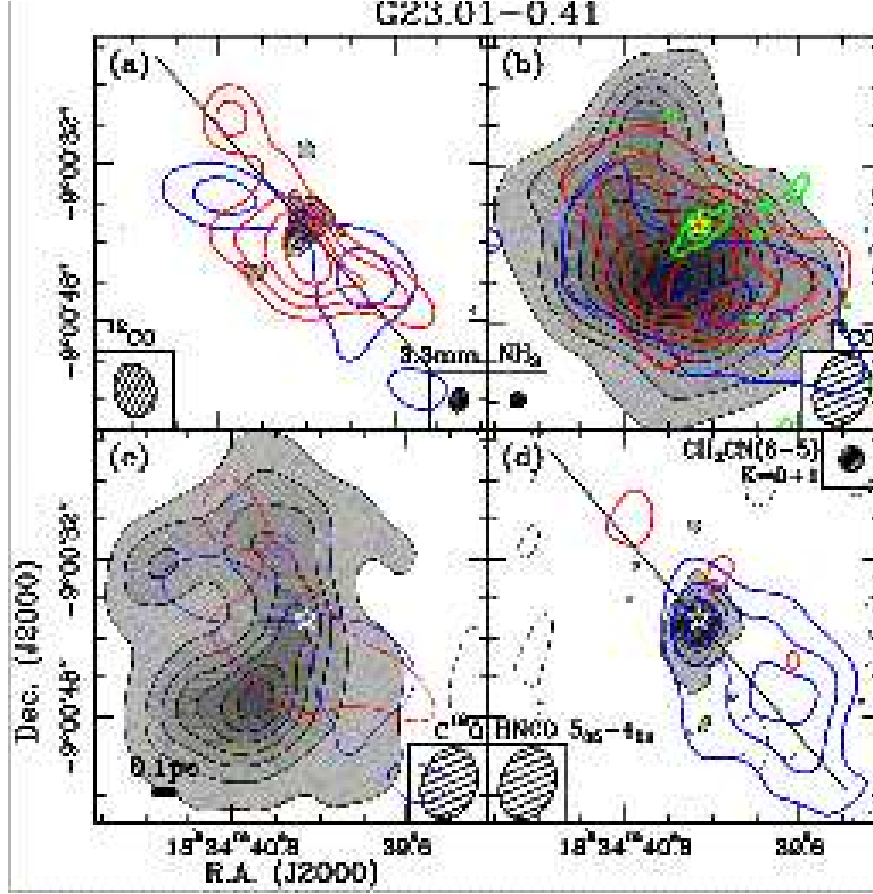


Fig. 6.— Maps of molecular lines and continuum emission for G 23.01–0.41: (a) overlay of blue- and redshifted wing emission maps of  $^{12}\text{CO}$  (1–0) on the 3 mm continuum emission (grey scale), (b) overlay of blue and redshifted wing emission maps of the  $^{13}\text{CO}$  (1–0), total integrated intensity maps of  $\text{NH}_3$  (2,2) (green contour; CTC97) on the integrated intensity map of the bulk  $^{13}\text{CO}$  (1–0) emission (grey scale plus contour;  $69.0 \leq V_{\text{LSR}}/\text{km s}^{-1} \leq 85.3$ ), (c) total integrated intensity map of  $\text{C}^{18}\text{O}$  (1–0) (grey scale;  $60.0 \leq V_{\text{LSR}}/\text{km s}^{-1} \leq 87.2$ ), and (d) overlays of the blue and redshifted  $\text{HNC O } 5_{05} - 4_{04}$  emission on the total map of  $\text{CH}_3\text{CN } (6-5) K=0+1$  emission (grey scale). The dashed contours correspond to the  $-3\sigma$  level for  $^{13}\text{CO}$  in panel (b),  $\text{C}^{18}\text{O}$  in (c), and  $\text{HNC O}$  in (d). The blue- and redshifted wing emission are integrated over the velocity ranges of  $49.9 \leq V_{\text{LSR}}/\text{km s}^{-1} \leq 71.5$  and  $86.0 \leq V_{\text{LSR}}/\text{km s}^{-1} \leq 101.6$  for  $^{12}\text{CO}$ ,  $47.2 \leq V_{\text{LSR}}/\text{km s}^{-1} \leq 69.0$  and  $85.3 \leq V_{\text{LSR}}/\text{km s}^{-1} \leq 96.2$  for  $^{13}\text{CO}$ ,  $48.1 \leq V_{\text{LSR}}/\text{km s}^{-1} \leq 69.9$  and  $86.2 \leq V_{\text{LSR}}/\text{km s}^{-1} \leq 91.6$  for  $\text{HNC O}$ , respectively (see also Figure 3c). All the contours and symbols are the same as in Figure 4. The RMS noise levels of the images are 90, 26, 1.4, 0.70, 0.79, 5.1, 21, 22 and 0.13  $\text{mJy beam}^{-1}$  for  $^{12}\text{CO}$  blueshifted,  $^{12}\text{CO}$  redshifted, 3 mm continuum,  $^{13}\text{CO}$ ,  $\text{C}^{18}\text{O}$ ,  $\text{NH}_3$ ,  $\text{HNC O}$  blueshifted,  $\text{HNC O}$  redshifted, and  $\text{CH}_3\text{CN}$  maps, respectively. All the other symbols are the same as in Figure 4.



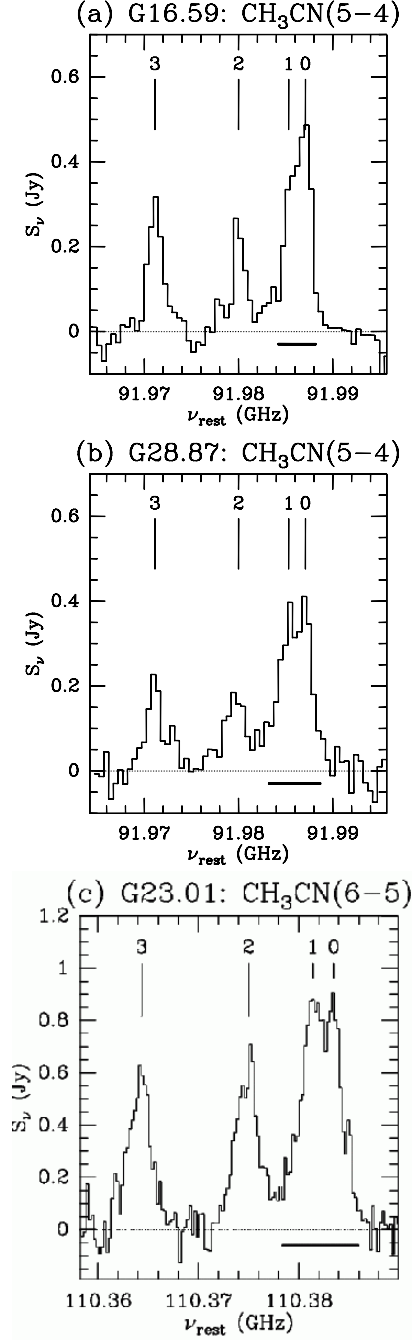


Fig. 7.— Mean  $\text{CH}_3\text{CN}$  spectra integrated over the  $5\sigma$  level areas of the 3 HMCs in flux density ( $S_\nu$ ) scale:  $J = 5-4$  for G 16.59–0.05 and G 28.87+0.07, and  $J = 6-5$  for G 23.01–0.41. The vertical bars above the spectra indicate the rest-frequency of the  $K$  rotational ladder emission. The horizontal bars under  $K = 0$  and 1 emission indicate frequency ranges to obtain the integrated intensity maps in the panels (d) of Figures 4 – 6.

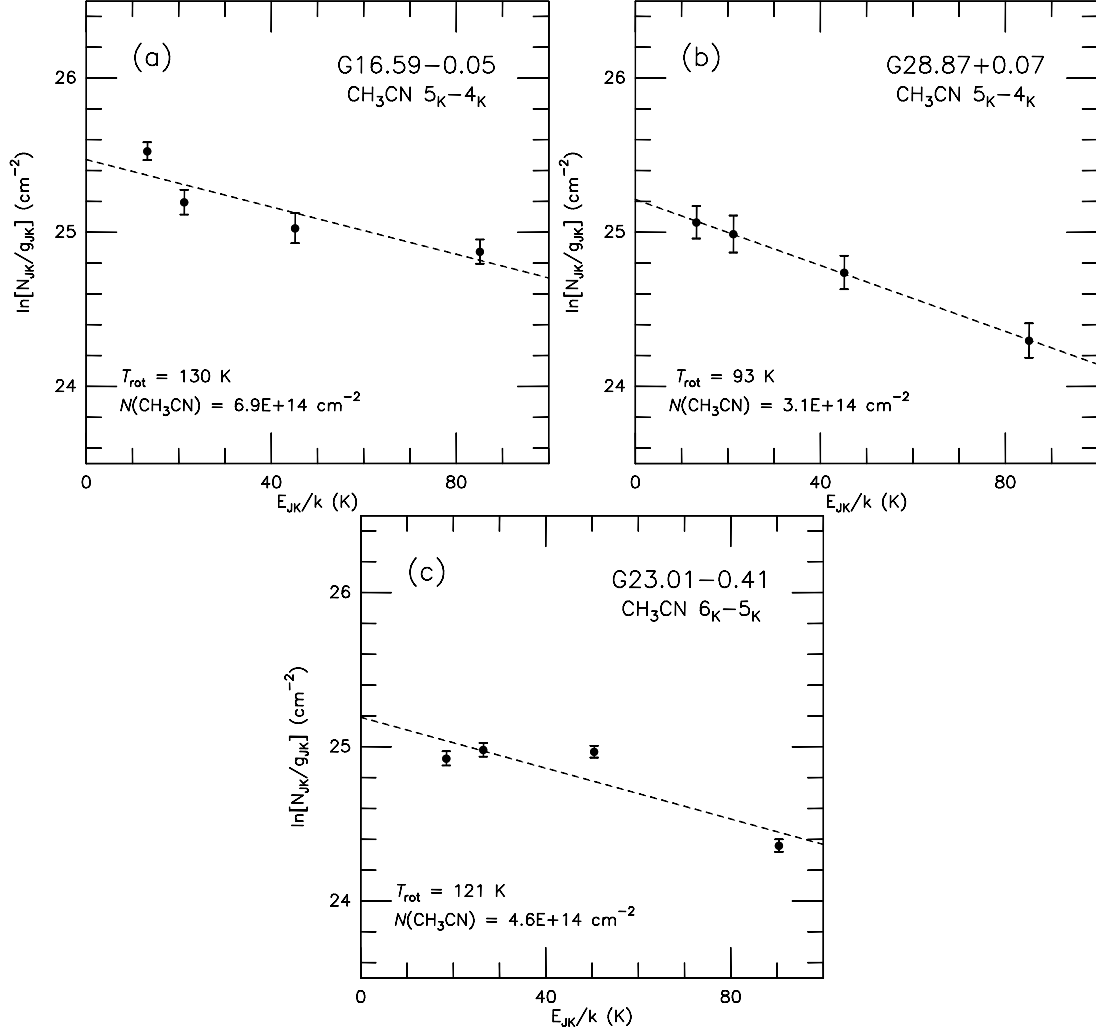


Fig. 8.— Rotational diagrams for CH<sub>3</sub>CN  $J_K \rightarrow (J-1)_K$  transitions obtained from the averaged spectra over the  $5\sigma$  areas of the  $K = 0 + 1$  emission (Figure 7), see §3.5.1. The natural logarithm of the column density in state  $J$  per substate  $[\ln(N_{JK}/g_{JK})]$  (cm<sup>-2</sup>) is plotted to the upper energy level of  $E_J/k$ . The dashed straight line is a least-square fit to the data, yielding rotational temperature ( $T_{\text{rot}}$ ) and column density,  $N(\text{CH}_3\text{CN})$ , shown in each panel. All the derived parameters are summarized in Table 9.

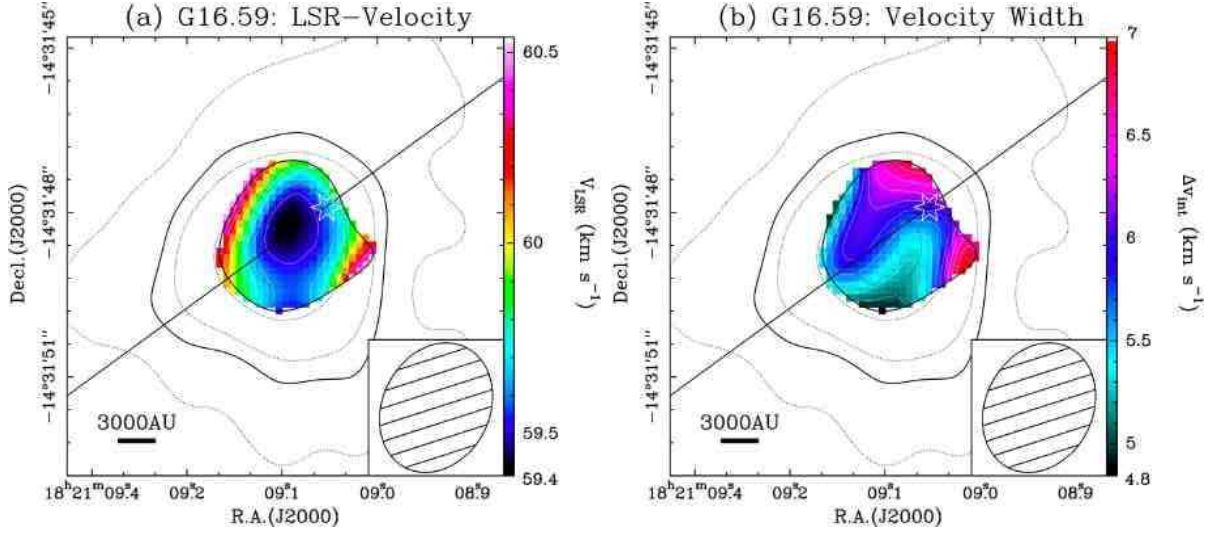


Fig. 9.— (a) Isovelocity and (b) intrinsic velocity width ( $\Delta v_{\text{int}}$ ) maps obtained from the multiple Gaussian line-profile fitting to the  $\text{CH}_3\text{CN}$  emission towards the central portion of the G 16.59–0.05 HMC. These maps are presented inside the  $5\sigma$  level contour (inner solid contour) of the  $K = 3$  total maps; the outer solid contour indicates the  $5\sigma$  level of the  $K = 0 + 1$  map. The dashed thin contours show the positive contour for the  $K = 0+1$  map in Figure 4. The ellipses at the bottom-right corners indicate synthesized beam size (Table 1). The straight lines and central stars are the same as in Figure 4. Systemic velocity ( $V_{\text{sys}}$ ) of the HMC is  $V_{\text{LSR}} = 59.8 \text{ km s}^{-1}$  (Table 8), and thermal line width at  $T_k = T_{\text{rot}} = 130 \text{ K}$  is  $0.38 \text{ km s}^{-1}$ .

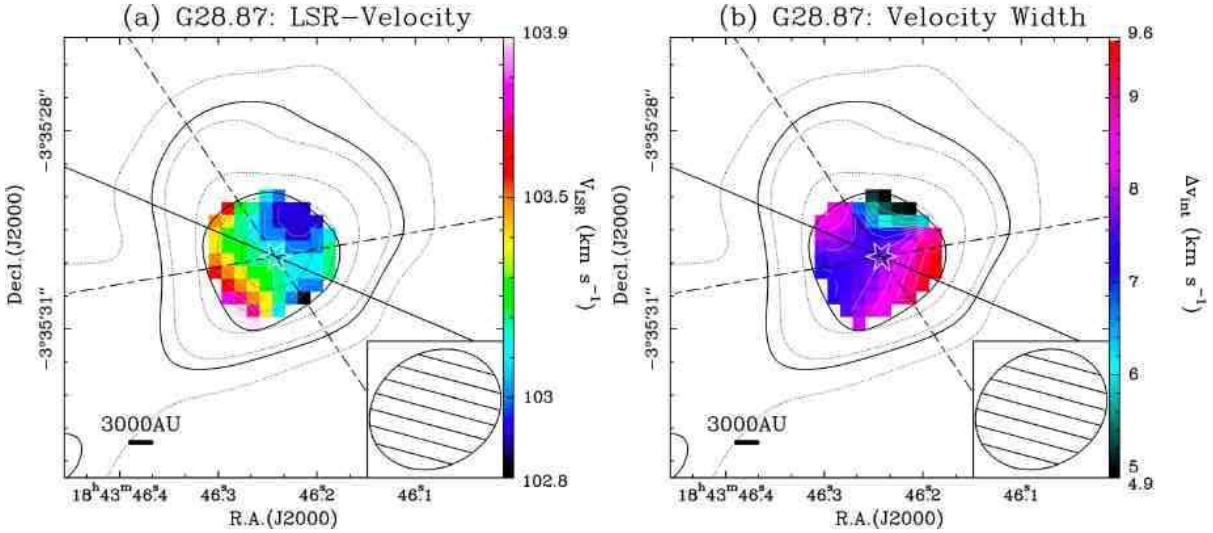


Fig. 10.— Same as Figure 9, but for G 28.87+0.07. The  $V_{\text{sys}}$  is  $V_{\text{LSR}} = 103.5 \text{ km s}^{-1}$  (Table 8), and thermal line width at  $93 \text{ K}$  is  $0.32 \text{ km s}^{-1}$ .

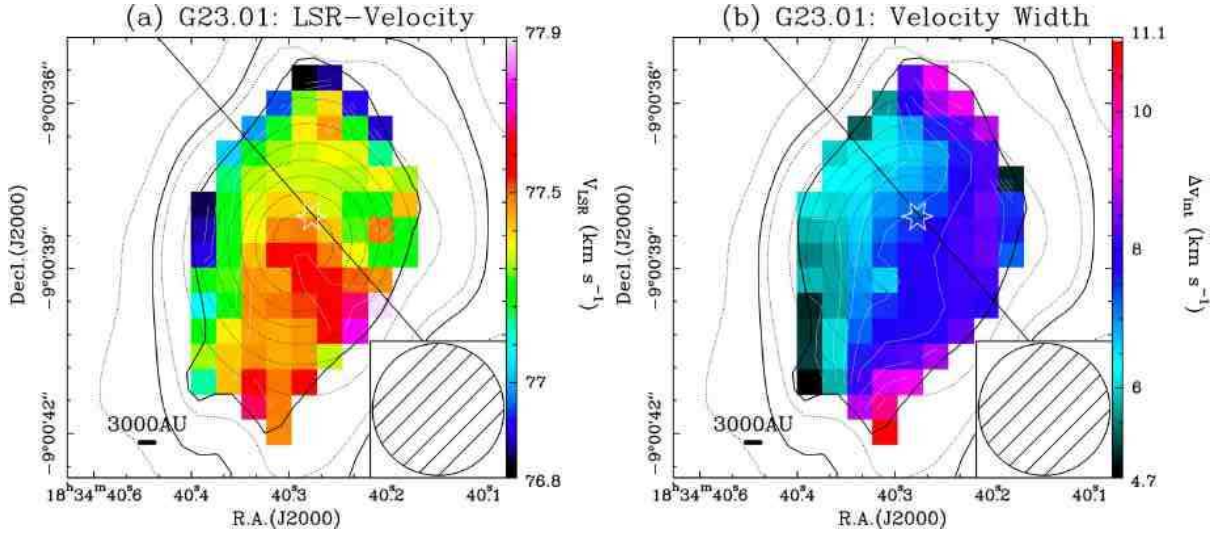


Fig. 11.— Same as Figure 9, but for G 23.01–0.41. The transition employed here is  $J=6-5$ . The  $V_{\text{sys}}$  is  $V_{\text{LSR}}=77.4 \text{ km s}^{-1}$  (Table 8), and thermal line width at 121 K is  $0.37 \text{ km s}^{-1}$ .